Agricultural and Forest Meteorology 372 (2025) 110684

Contents lists available at ScienceDirect

Agricultural and Forest Meteorology

journal homepage: www.elsevier.com/locate/agrformet

Evaluation of a novel approach to partitioning respiration and photosynthesis using eddy covariance, wavelets and conditional sampling

Pedro Henrique H. Coimbra [a,*], Benjamin Loubet [a], Olivier Laurent [b], Matthias Mauder [c,d], Bernard Heinesch [e], Jonathan Bitton [e], Nicolas Delpierre [f,g], Daniel Berveiller [f], Jérémie Depuydt [a], Pauline Buysse [a]

[a] ECOSYS, INRAE, AgroParisTech, Université Paris-Saclay, Palaiseau, France
[b] Laboratoire des Sciences du Climat et de l'Environnement, CEA, CNRS, Université Paris-Saclay, Gif-sur-Yvette, France
[c] Institute of Meteorology and Climate Research - Atmospheric Environmental Research (IMK-IFU), Karlsruhe Institute of Technology, Garmisch-Partenkirchen, Germany
[d] Institute of Hydrology and Meteorology, Technische Universität Dresden, Dresden, Germany
[e] Faculté des Sciences Agronomiques de Gembloux, Unité de Physique, Gembloux, Belgium
[f] Ecologie Systématique Evolution, CNRS, AgroParisTech, Université Paris-Saclay, Gif-sur-Yvette, France
[g] Institut Universitaire de France, France

ARTICLE INFO

Keywords:
Eddy-covariance
Wavelet
CO2 flux
Partitioning
Photosynthesis
Respiration

ABSTRACT

The eddy covariance (EC) technique remains a cornerstone for direct, continuous monitoring of greenhouse gases fluxes, particularly for carbon dioxide (CO_2). Traditionally, EC-derived net ecosystem exchange (NEE) is partitioned into gross primary productivity (GPP) and ecosystem respiration (R_{eco}) using model-based approaches. Here, we present a novel, fully empirical partitioning method that applies conditional sampling to wavelet-decomposed signals, isolating positive and negative contributions of the wavelet co-spectrum of vertical wind velocity and CO_2 dry molar fraction, conditioned by the water vapour flux. This method was evaluated across two French ICOS sites, a mixed forest (FR-Fon) and a cropland (FR-Gri), over multiple years.

The approach is grounded in the hypothesis that wavelet decomposition enables separation of oppositely signed turbulent structures across scales, a claim supported by co-spectral analysis. The resulting flux components exhibited distinct frequency signatures under neutral and unstable atmospheric conditions, though not under stable stratification.

Daily partitioned fluxes derived from this method aligned well with GPP and R_{eco} estimates from established nighttime- and daytime-based partitioning, with inter-method differences smaller than those observed between the conventional approaches themselves. Conceptually the method approximates net photosynthesis and offered improved coherence with site-specific ecological and management dynamics, capturing events such as growing season, harvest, and manure application at FR-Gri, more reliably than standard methods. It also avoided spurious GPP estimates common error in the night-time approach. Moreover, the diel R_{eco} cycle revealed a bimodal pattern, suggestive of combined influences from solar radiation and soil temperature, in contrast to the predominantly single temperature-driven dynamics inferred by conventional models.

Our findings demonstrate that wavelet-based conditional sampling offers a promising alternative for CO_2 flux partitioning, one that is entirely empirical, calibration-free, and grounded in the physical co-emission dynamics and transport from surface to the atmosphere.

1. Introduction

Global surface temperature is 1.1 °C warmer compared with the pre-industrial era, even larger on land (1.6 °C) (IPCC, 2021). Climate change leads to widespread adverse impacts and related losses and damages to nature and people (IPCC, 2022b). Projections show >2 °C warming in 2100 due to mismatches between implemented policies and long-term goals (IPCC, 2022a). The warming results from the increase in greenhouse gas (GHG) concentration in the atmosphere, which is, in turn, the result of anthropogenic emissions (IPCC, 2021). The largest share of

* Corresponding author.
E-mail address: pedro-henrique.herig-coimbra@inrae.fr (P.H.H. Coimbra).

https://doi.org/10.1016/j.agrformet.2025.110684
Received 19 October 2023; Received in revised form 16 May 2025; Accepted 4 June 2025
Available online 17 June 2025

these emissions (86 %) comes from fossil fuel CO_2 emissions (9.6 ± 0.5 Pg C yr^{-1}) (Canadell et al., 2021). While stopping these emissions should remain the first objective, mitigating climate change will require decreasing all GHG sources. Agriculture, forestry and other land use (AFOLU) is a significant source of GHG (12.0 ± 2.9 GtCO2eq yr^{-1}) (Jia et al., 2019). However, it has the potential to remove CO_2 from the atmosphere. Indeed, carbon uptake by vegetation has increased over the past decades, but uncertainties remain about whether this trend will continue (Canadell et al., 2021). Considering these uncertainties, soil carbon sequestration in croplands and grasslands has a considerable potential for removing CO2 from the atmosphere (0.4–8.6 GtCO2eq yr^{-1}) (Jia et al., 2019). Measuring and separating the different processes of land-atmosphere carbon flux is crucial to advise and monitor policies and goals effectively. Doing it, however, is not trivial.

The international scientific community is leveraging advanced techniques to produce reliable surface-atmosphere GHG flux monitoring. Eddy Covariance (EC) is praised for directly and continuously measuring surface turbulent fluxes. Since the early measurements, the method has been applied to different gases, including water vapour, CO_2, CH_4 and N_2O (Valentini et al., 1996; Moncrieff et al., 1997; Fowler et al., 1995). Active development of instrumentation and standardization of the methods and networks has made it the reference measurement for terrestrial ecosystem GHG fluxes (Pastorello et al., 2020).

Eddy covariance has been employed on fixed towers and airborne measurements, where non-stationarity is a frequent challenge. Non-stationarity poses a significant limitation for the conventional eddy covariance method. To address this, alternative methods that resolve surface fluxes in both time and frequency have been developed for situations where stationarity cannot be guaranteed, such as in airborne measurements (Strunin and Hiyama, 2004; Mauder et al., 2007; Desjardins et al., 2018; Metzger et al., 2013). These methods have also been used to capture outbursts and non-stationary CH_4 fluxes (Schaller et al., 2017; Göckede et al., 2019). In the examples above, fluxes were non-stationary but could be calculated due to the use of wavelet transform, which decomposes a signal in time and scale (Mallat, 1989; Farge, 1992; Farge and Schneider, 2001), whereas calculating flux based on Gaussian statistics is not permissible. By dealing with non-stationarity, they yield high-quality data with fewer gaps, hence, more available data for analysis to feed gap-filling algorithms and further partitioning.

EC measurements provide the net turbulent surface flux, which is often the primary information we are interested in However, often enough, we need to partition CO_2 flux (Net Ecosystem Exchange, NEE) into gross primary productivity (GPP) and ecosystem respiration (R_{eco}). The need comes because they are modelled in surface models, which we desire to calibrate under varying environmental forcing variables, mainly temperature, radiation, soil moisture and air humidity (Duffy et al., 2021).

Standard methods for NEE partitioning involve using photosynthetically non-active periods to estimate R_{eco} and further extrapolate it (night-time method) or use a light-response model for GPP (day-time method) (Reichstein et al., 2012). Alternative partitioning methods exist. Notable effort has been made to use high-frequency data (Thomas et al., 2008; Scanlon and Sahu, 2008; Scanlon and Kustas, 2010; Klosterhalfen et al., 2019a; Zahn et al., 2022). Despite the differences, they all share the idea of using the correlation between CO_2 and H_2O mixing ratios in the partitioning. The method proposed by Thomas et al. (2008) assumes that, during daytime, the Reynolds instantaneous deviations of CO_2 and H_2O concentrations exhibit opposite signs when air parcels originate from the plant crown, where photosynthesis dominates, and similar signs when originating from the ground, where respiration is the prevailing process. Thomas et al. (2008) refine a relaxed eddy accumulation approach to compute the ground respiration from the updraft measurements. They found that the partitioning quality depends on canopy height and leaf area index (Klosterhalfen et al., 2019a). The Scanlon et al. (2019) method uses flux-variance similarity to partition CO_2 and H_2O fluxes into stomatal and non-stomatal components simultaneously. The method relies on an estimated water use efficiency (WUE), making it not fully direct. In addition to this, an experiment has shown that even with true WUE, additional correction factors are required to get to the true partitioning, but this could only be achieved in the special case of the large eddy simulation experiments (Klosterhalfen et al., 2019b). Following up on Scanlon et al. (2019), Zahn et al. (2022) circumvent the water use efficiency by finding the ratio between evaporation and transpiration using the octant analysis in Thomas et al. (2008). There are mathematical constraints for Zahn's method when photosynthesis and respiration fluxes are close to zero or nearly balanced, and the same applies to evaporation and transpiration.

These methods have been tested with varying results (Scanlon and Kustas, 2012; Sulman et al., 2016; Wang et al., 2016; Perez-Priego et al., 2018; Rana et al., 2018; Zeeman et al., 2013). A comparison between methods showed that Scanlon and Kustas (2010) overestimates and Thomas et al. (2008) underestimate soil flux components (Klosterhalfen et al., 2019a). Note that all these partitioning methods operate solely in the time domain and use concentrations without explicitly accounting for eddy size or their timescale. While Scanlon and Albertson (2001) characterized the spatial scales of CO_2-enriched air parcels from temporal measurements using Taylor's frozen turbulence hypothesis, their approach was not applied as a direct partitioning method.

We notice that Thomas et al. (2008) found that the majority of sampled respiration events were attributed to small-scale eddies smaller than 0.1 s or even 0.05 s, which they explained by air coming from the ground having more time to being mixed by turbulence "leading to a dissection of formerly confined respiration pulses". Also, Scanlon and Albertson (2001) identified the sizes of eddies responsible for transporting air enriched in CO_2 from the forest floor to the atmosphere using wavelet analysis. They found that eddies around 8 m in diameter are most effective at transporting CO_2 from below the canopy. While these authors investigate the scales of turbulent transport of CO_2 and water vapour, neither directly calculates time-scale resolved fluxes. We hypothesise that time-scale resolved fluxes could help improve conditional sampling by separating respiration events efficiently.

We first present the wavelet-based framework for turbulent flux calculation. We then evaluate the new partitioning method by comparing it to the commonly used nigh-time partitioning method (Reichstein et al., 2005) partitioning method. We use two datasets from contrasted ICOS ecosystem sites in a single climatic region, with four years (2019–2022) from a deciduous mixed forest site (FR-Fon) and two years (2021–2022) from a crop site (FR-Gri).

2. Material and methods

In this work, we processed EC data from two ICOS sites. Both sites were treated equally and passed through the same processing steps (Fig. 1).

2.1. Site description

The study uses data from two French sites in the Parisian region and part of the ICOS network (https://www.icos-cp.eu) and FLUXNET. Climatically, the area can be described as oceanic with mild temperatures (11.2–11.5 °C annual mean) and moderately wet (677–700 mm annual precipitation).

The first site, FR-Gri (Buysse et al., 2024), is a 19-hectare crop site (Loubet et al., 2011), rotating between maize, wheat, barley, and rapeseed with intermediate crops. The measuring system is set up on a short tower that moves from 2 to 4 m according to the crop growth. We used data from January 2021 to December 2022 from this site, consisting of winter rapeseed until 31 July 2021, winter wheat from 7 October 2021 to 5 July 2022, and barley seeded on 11 October 2022. The second site, FR-Fon (Berveiller et al., 2024), is a deciduous broadleaf mixed forest mainly composed of oak and hornbeams (Delpierre et al., 2016). The oaks have a dominant height of 30 m, while the largest

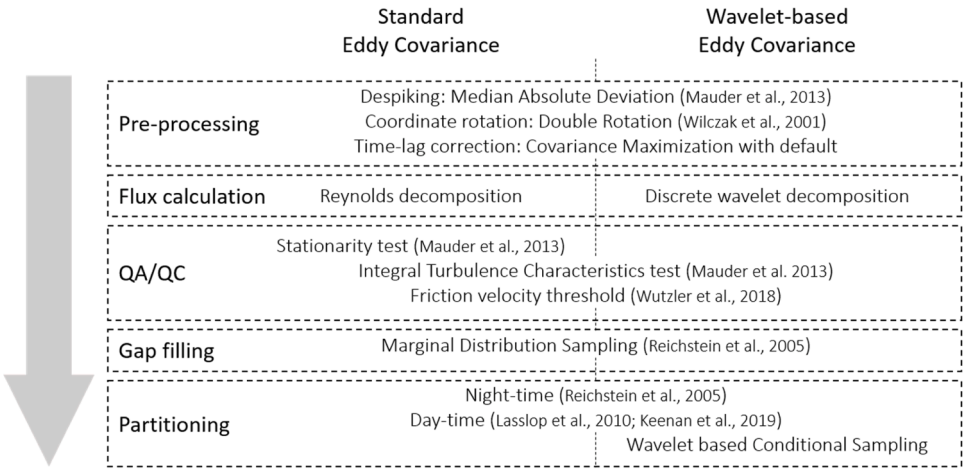

Fig. 1. Processing steps in standard and wavelet-based eddy covariance in this work.

hornbeams reach a height of 20 m, and the Leaf Area Index (LAI) is distributed with 70 % Oak and 30 % Hornbeam. The eddy covariance setup is located at 37 m above ground. From this site, we used data from January 2019 to December 2022.

In both sites, the Eddy Covariance setup consisted of a closed-path infrared gas analyser (LI-7200; Li-Cor Inc., Lincoln, NE, USA) and a three-dimensional sonic anemometer (Gill HS; Gill Instruments Ltd, Lymington, Hampshire, UK). Both instruments and acquisition setups followed ICOS guidelines and protocols (Sabbatini et al., 2018).

2.2. EC flux processing

To compute the atmosphere-biosphere flux, we consider a virtual rectangle box extending from the ground to the location of the eddy-covariance setup of width W, length L and height h_m. The mass balance of a scalar in the virtual box is used to retrieve F_{eco} (μmol m^{-2} s^{-1}), the overall ecosystem flux. The mass balance includes a storage term (I), an advection transport term (II) and a turbulent diffusion term (III), which, when integrated over the three dimensions of the virtual box, equals (Foken et al., 2012; Metzger, 2018; Aubinet et al., 2005; van Gorsel et al., 2009):

$$0 = \int_{-L}^{L}\int_{-W}^{W}\int_{0}^{h_m}\left[-S + \underbrace{\overline{\rho_d}\frac{\partial\overline{\chi_s}}{\partial t}}_{I} + \underbrace{\overline{\rho_d u}\frac{\partial\overline{\chi_s}}{\partial x} + \overline{\rho_d v}\frac{\partial\overline{\chi_s}}{\partial y} + \overline{\rho_d w}\frac{\partial\overline{\chi_s}}{\partial z}}_{II} + \underbrace{\frac{\partial\overline{\rho_d u'\chi_s'}}{\partial x} + \frac{\partial\overline{\rho_d v'\chi_s'}}{\partial y} + \frac{\partial\overline{\rho_d w'\chi_s'}}{\partial z}}_{III}\right] dz\,dx\,dy \quad (1)$$

Where S is the ecosystem volumetric flux (μmol m^{-3} s^{-1}), ρ_d the dry air molar density (mol m^{-3}), χ_s the scalar dry mole fraction (μmol mol^{-1}), t the time (s), while u, v and w are the upwind, crosswind and vertical component of the windspeed (m s^{-1}). Overbars indicate time averaging; quotation marks the instantaneous deviation from the mean. Assuming a horizontally homogeneous ecosystem (homogeneity in ecosystem functioning and structure over x and y) allows suppressing the horizontal derivatives and integrals in Eq. (1) (Finnigan et al., 2003; Metzger, 2018). This assumption also leads to a zero dry air vertical flux due to continuity $\overline{\rho_d w} = 0$ (Webb et al., 1980). Then, recognising that the integral of S over the height z is $F_{eco} - F_{soil}$ and that, similarly, the integral of $\frac{\partial\overline{\rho_d w'\chi_s'}}{\partial z}$ over z is $\overline{\rho_d w'\chi_s'} - F_{soil}$, Eq. (1) leads to:

$$F_{eco} = \overline{\rho_d}\cdot\left(\int_0^{h_m}\frac{\partial\overline{\chi_s}}{\partial t}dz + \overline{w'\chi_s'}\right) \quad (2)$$

Where $\overline{w'\chi_s'}$ is the turbulent flux at h_m. The ecosystem flux can hence be evaluated from $\overline{w'\chi_s'}$ and the storage term ($\int_0^{h_m}\frac{\partial\overline{\chi_s}}{\partial t}dz$), which may be significant in medium and tall towers but can be neglected in small ones. In practice, $\overline{w'\chi_s'}$ is computed from a time series of w and χ_s and sampled at a frequency typically higher than 5 Hz to capture the smallest eddies contributing to the flux (Gu et al., 2012).

In this study, we use two methods to evaluate $\overline{w'\chi_s'}$: the standard eddy covariance method (EC_S), and the Discrete Wavelet Transform (DW-EC).

From w and χ_s, the standard method consists of calculating the product of the instantaneous deviations of both variables from their respective means (covariance); time-frequency resolved methods work the same, using, however, previously decomposed instantaneous deviation (Fig. 2).

2.2.1. Data pre-processing

In this study, data flux pre-processing was done using EddyPro 7.0.9.

For all flux calculations, we applied de-spiking (Mauder et al., 2013), covariance maximization for time lag correction, and double rotation for tilt correction (Wilczak et al., 2001). The default time lag was set to 0.4 s for CO_2 and 0.7 s for H_2O for a 71.1 cm tube with a 5.3 mm inner diameter and 15 L/min flow rate. These values were allowed to vary between 0.15 to 0.65 s for CO_2 and 0.2 to 1.2 s for H_2O. Using closed path systems and dry mixing ratios for gas avoids compensating for density fluctuations (Kowalski and Serrano-Ortiz, 2007). No detrending was applied. Standard flux calculations require further corrections to address low and high-frequency losses (Massman and Lee, 2002). These spectral corrections are usually applied after flux calculation and can significantly impact the carbon budget. On average, the correction factor remains below 5 % for CO2 and below 20 % for H_2O. However, it can sometimes increase the absolute flux by up to 15 % for CO_2 and 80 % for H_2O (Polonik et al., 2019).

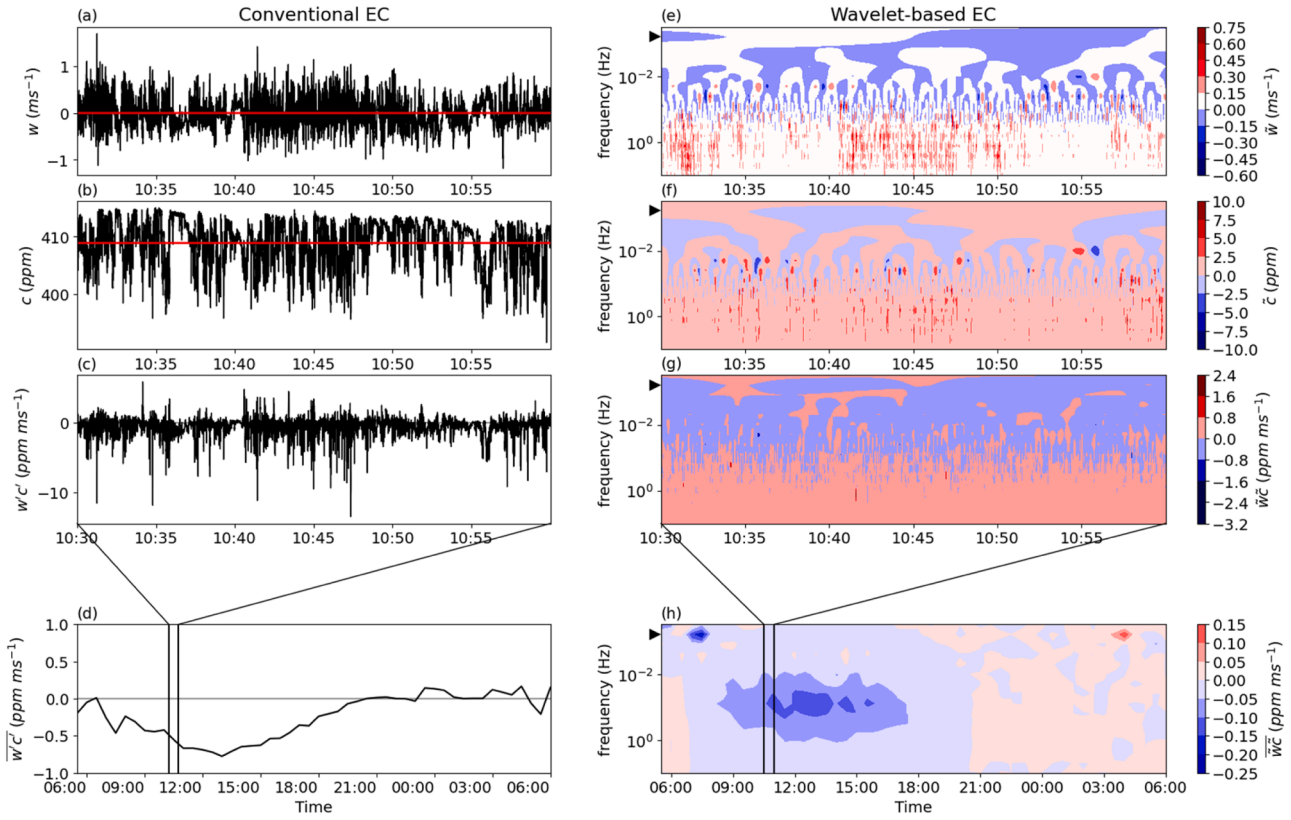

Fig. 2. Step-by-step visualisation of the standard and wavelet-based eddy covariance methods. The triangle in e-h panels indicates the frequency equivalent to 30 min. Here, w refers to vertical wind speed (m s^{-1}), c refers to the CO_2 mixing ratio (ppm), and $\overline{w'\chi_s'}$ and $\overline{\tilde{w}_j\tilde{\chi}_{sj}}$ are in units of ppm m s^{-1}. The data shown is from FR-Gri, covering the period from May 13, 2022, 05:30 to May 14, 2022, 06:00.

Here, for simplicity's sake and since we are focusing on comparing the flux calculation, gap filling and partitioning methods rather than interpreting the fluxes themselves, these corrections were omitted.

2.2.2. Standard eddy covariance (EC_S)

The eddy covariance method consists of calculating the covariance $\overline{w'\chi_s'}$ (Fig. 2). Typically, fluxes are calculated every 30 min to 1 hour (Rebmann et al., 2018; Pastorello et al., 2020; Aubinet et al., 1999). The time average should be chosen to effectively capture the turbulent signal while isolating it from the influence of larger atmospheric structures. Turbulent fluctuations χ_s' and w' are formally defined as deviations from an ensemble average and not from a time average. The ergodic assumption is required to make the ensemble and time average equivalent. Thus, for methodological reasons, the averaging period should also be stationary and sufficiently long to gather enough data to get a low random error (Kaimal and Finnigan, 1994). In general, a 30-minute period satisfies these requirements.

2.2.3. Wavelet transform methods

Wavelet transform is a mathematical method to decompose a time series in time and frequency. The following steps explain how to perform a time-frequency resolved covariance using wavelets (Fig. 2). More details can be found in (Daubechies, 1992; Farge, 1992; Mallat, 1999; Farge and Schneider, 2001).

Any signal $f(t)$ can be decomposed into different scales, which results in the signal itself once added up. The simplest example is the Reynolds decomposition that separates a time series into its mean and its instantaneous deviation:

$$\boldsymbol{f}(\boldsymbol{t}) = \boldsymbol{f}'(\boldsymbol{t}) + \overline{\boldsymbol{f}(\boldsymbol{t})} \tag{3}$$

In Eq. (3), the mean, $\overline{f(t)}$, is the low-frequency component, with a frequency representative of 1/T, where T is the averaging period. Similarly, a time series can be decomposed into its frequency f:

$$\boldsymbol{f}(\boldsymbol{t}) = \int_{f=0}^{\infty} \boldsymbol{f}(\boldsymbol{t},\boldsymbol{f}) = \sum_{j=0}^{J} \boldsymbol{f}(\boldsymbol{t},\boldsymbol{j}) \tag{4}$$

The wavelet transform is a way to decompose the signal using a mother wavelet ψ, a wave function (Eq. (5)). The decomposition can be continuous (CWT; Torrence and Compo, 1998) or discrete (DWT). A great interest in the DWT is that the orthogonality and the progressively smaller decomposition make it far cheaper computationally than CWT at the expense of a coarser resolution in frequency (Mallat, 1989). DWT is, therefore, a good candidate for a time series that lasts more than a couple of weeks. More so, the independence between frequencies simplifies the flux's computation by covariance, which would otherwise have to consider cross-covariance between variables and frequencies (see Eq. (12)). We will only consider DWT in this manuscript.

Considering N discrete observations with a sampling period δ_t, so that $t = n\ \delta_t$ where n and n' are time indexes, we can generate a family of wavelets:

$$\boldsymbol{\psi}_{\boldsymbol{n},\ \boldsymbol{j}}(\boldsymbol{n}') = \boldsymbol{s}_{\boldsymbol{j}}^{-1/2}\boldsymbol{\psi}\left[\frac{(\boldsymbol{n}'-\boldsymbol{n})\boldsymbol{\delta}_{\boldsymbol{t}}}{\boldsymbol{s}_{\boldsymbol{j}}}\right] \tag{5}$$

Where j represents a scale, s_j is the scaling factor, usually defined using a geometric progression with a maximum limited by the total sampling period $N\delta t$: $s_j = s_0 2^{j\delta_j}$, for $j = 0,1,\ldots J$. Here, J is the size of the set of scales, s_0 is the smallest resolvable scale, approximately $2\delta t$, and δ_j is the scale factor equal to 1 for discrete wavelets with orthogonal base (Farge, 1992). Orthogonality ensures independent frequencies and implies:

$$\sum_{n'} \psi_{n,j}(n')\psi_{m,i}(n') = 0 \textit{ if } i \neq j \textit{ or } n \neq m,\ 1 \textit{ otherwise} \quad (6)$$

Where m is the time index equivalent to n, and i is a scale equivalent to j. Note that the independent-frequencies property, where the correlation between different scales vanishes, is valid only for orthogonal wavelet transform and when the averaging time matches at least the time-support of the transform; for instance, the correlation between scales will persist if the averaging time is too short. The inner product of the signal $f(n)$ with a scaled mother wavelet ψ, yields the $W(n,j)$, the wavelet coefficient for time series $f(n)$: $W(n,\ j) = \sum_{n'=0}^{N-1} f(n')\psi_{n,\ j}(n')$. We can reconstruct the signal in time-frequency dimensions as:

$$\widetilde{f}(n,j) = \sum_{n'=0}^{N-1} W(n,\ j)\ \psi_{n,j}(n') \quad (7)$$

Where $\widetilde{f}(n,\ j)$ is the decomposed signal defined in both time and frequency. The fully reconstructed signal is then found by summing to infinity the components of the decomposed signal:

$$f(n) = \sum_{j=0}^{\infty} \widetilde{f}(n,j) \quad (8)$$

A limiting scale J can be introduced to define a low-frequency component $A_J(n)$, known as the approximation coefficient, which aggregates all scales below J. In essence, J is selected such that A_J represents the result of a low-pass filter capturing the frequency range (0, 1/T), where T is typically 30 min.

$$f(n) = \sum_{j=0}^{J} \widetilde{f}(n,j) + A_J(n) \quad (9)$$

Then, if for a time average T, we assume $\overline{f(n)} \approx A_J$, where $\overline{f(n)} = \frac{1}{T}\sum_{n=1}^{1/T} f(n)$ and J in A_J represents the scale in which $s_J = T$, then from (3), we have:

$$f'(n) = f(n) - \overline{f(n)} \approx \sum_{j=0}^{J} \widetilde{f}(n,f) \quad (10)$$

Note that, in fact $A_J(n)$ is different from $\overline{f(n)}$, as it is time-dependent and can be seen as a low-pass filter. Actually, for a trendless time series $\overline{A_J(n)} = \overline{f(n)}$. Based on Eq. (10), and considering the orthogonality of discrete wavelets, which implies Eq. (6), we can compute the turbulent flux from Eq. (2) as:

$$F_c = \overline{\rho_d}\overline{w'\chi'_s} = \overline{\rho_d}\sum_{j=0}^{J} \widetilde{w_j}\widetilde{\chi_{sj}} \quad (11)$$

In this study, we applied discrete decomposition using the Daubechies wavelet with 6 filter coefficients (db6) (Daubechies, 1988). For comparisons with the standard eddy covariance method, we compute the covariance by summing scales s_j smaller than 1800 s (30 min). Calculations were done using the *PyWavelets* module (Lee et al., 2019).

Fig. 2 illustrates the steps of the standard EC calculation with the time-frequency decomposition of *w*, *c*, and their product at 20 Hz over 20 min and the 30-minute covariance over a whole day.

2.2.4. Cone of influence

Wavelet coefficients calculated with the inner product in Eq. (6) are subject to the influence of neighbours, resulting in a time "influence cone" that grows with decreasing frequency. This cone renders the reconstruction unusable at the edges of the dataset and for scaling factors close to the dataset duration. Note that in Fig. 2, e-h panels, the cone of influence is outside of the plot.

The maximum scale J where at least one of the wavelet coefficients is unaffected by edge effects can be calculated for discrete wavelets as:

$$J_{max} = \left\lfloor \log_2\left(N \Big/ \left(f_{length} - 1\right)\right)\right\rfloor \quad (12)$$

Where f_{length} is the filter length, which is 12 for *db6*.

Based on Eq. (12) we selected the 20 h of data centred in the half hour to calculate each half hour. After wavelet calculation, we selected only the central half-hour, guaranteeing that with this extension a set of scales s_j with unaffected coefficients up to 9.3e^{-5} Hz (3 h).

2.3. Timeseries flagging and gap-filling

Previous steps allowed us to calculate $\overline{w'\chi_s'}$, where χ_s is represented as c for CO_2 and v for H_2O. We must still verify the EC's assumptions through a quality check (Fig. 1). Non-stationarity data for standard EC and periods lacking turbulence for both standard and wavelet-based EC are considered unreliable and thus flagged out and gap-filled.

2.3.1. Quality flags

Quality flags followed the standard 0-1-2 flag system used in FLUXNET (Mauder and Foken, 2011). The system is based on two tests, one for stationarity and another to verify that turbulence is fully developed (Foken and Wichura, 1996).

In the standard eddy-covariance approach, stationarity is required so that the time average is approximately the ensemble average. The ensemble average is, in theory, needed but, in practice, not obtainable as it would require random experiments.

The stationarity test (STA) calculates the absolute relative deviation between the mean of the covariances computed over 5-min intervals and the covariance computed over a 30-min period:

$$STA = \left| \frac{\frac{1}{6}\sum_{i=1}^{6} \overline{(w'\chi'_s)_i^{5-mn}} - \overline{(w'\chi'_s)^{30-mn}}}{\overline{(w'\chi'_s)^{30-mn}}} \right| \quad (13)$$

The turbulence test, or integral turbulence characteristics (ITC) test, identifies if eddies are fully developed by calculating the absolute relative deviation between the measured and modelled integral turbulent characteristic σ_w/u_*. The model is calculated as

$$(\sigma_w/u_*)^{model} = \begin{cases} 0.21\ln\left(\frac{z+f}{u_*}\right) + 3.1, & if\ -0.2 < z/L < 0.4 \\ 2\left(\frac{z}{L}\right)^{1/8}, & else \end{cases} \quad (14)$$

Where f is the Coriolis parameter (s^{-1}), u_* is the friction velocity (m/s), z is the height (m), L is the Obukhov length (-), and z+ is set to 1 meter for a mathematical convention so that $\frac{z+f}{u_*}$ is dimensionless (Thomas and Foken, 2002).

$$ITC = \left| \frac{(\sigma_w/u_*)^{model} - (\sigma_w/u_*)^{measurement}}{(\sigma_w/u_*)^{measurement}} \right| \quad (15)$$

A detailed description of the quality control procedures can be found in Foken and Wichura (1996) and Mauder and Foken (2011). Data is considered high-quality (flag = 0) when this deviation is below 30 % for all applicable tests, medium-quality (flag = 1) when at least one test falls between 30 % and 100 %, and low-quality (flag = 2) when any test exceeds 100 %.

2.3.2. u* Filtering

Further screening is necessary to discard observations below a friction velocity threshold (u^*_{crit}) (Wutzler et al., 2018; Papale et al., 2006). Under stable stratified atmospheric conditions, the EC technique has been shown to underestimate nocturnal CO_2 respiration (Goulden et al., 1996; Baldocchi, 2003). The reason is that the turbulence is attenuated by the positive air density gradient (Kaimal and Finnigan, 1994). As

biotic flux is not expected to depend on turbulence, we can define a threshold value for friction velocity (u^*_{crit}) below which the measured ecosystem CO_2 flux starts to decrease. Below u^*_{crit} turbulence is not developed enough to mix the surface layer and the EC to perform well. This method provides an alternative way to determine the turbulent requirement based on an ecosystem function instead of using a physical-based one, as with ITC. Once a threshold is defined, observations below this threshold are dropped and gap-filled (Gu et al., 2005; Aubinet et al., 2012). The u_* threshold was determined using the *ReddyProc* library in R and was free to vary among seasons (Wutzler et al., 2018).

2.3.3. Gap-filling

Gap-filling was performed on data flagged for medium (1) and low (2) quality or below u*crit. For EC_S, both stationary and turbulence flags were considered. Following Mauder et al. (2007), DW-EC only considered the turbulence flag. We used the Marginal Distribution Sampling (MDS) method, the most commonly used gap-filling method (Pastorello et al., 2020). MDS involves sampling data from the temporal vicinity of the data to be gap-filled, typically using a 15-day window. Similar meteorological conditions are defined by incoming shortwave radiation, air temperature, and vapour pressure deficit. This subset yields a distribution function used to fill the gap, exploiting both the meteorological drivers and the temporal auto-correlation structure of NEE (Reichstein et al., 2005). For the calculations, we used the *ReddyProc* library in R (Wutzler et al., 2018).

2.4. NEE partitioning

Flux partitioning refers to the division of the Net Ecosystem Exchange (NEE) into the ecosystem respiration (R_{eco}) and the gross primary productivity (GPP). Ecosystem respiration refers to the release of CO_2 by organisms during their metabolic activities, including autotrophic respiration by plants and heterotrophic respiration by micro- and macro-organisms in soil and the ecosystem. GPP represents the uptake of CO_2 by plants through photosynthesis:

$$\boldsymbol{NEE} = \boldsymbol{GPP} + \boldsymbol{R_{eco}} \tag{16}$$

GPP is a CO_2 flux directed from the atmosphere to the ecosystem (negative), while R_{eco} is from the ecosystem to the atmosphere (positive).

In standard practice, partitioning relies on the presumed responses of GPP and R_{eco} to light, water, and temperature. We applied the known night- and day-time methods on both standard and wavelet-based CO_2 fluxes and proposed a new method for the wavelet-based flux here.

2.4.1. Night-time partitioning method

Night-time (NT) partitioning assumes that GPP is zero at night, so NEE equals R_{eco} (Reichstein et al., 2005). Reference respiration rate and temperature sensitivity are then parametrized using an Arrhenius-type temperature response model for nocturnal measurements and projected into the day (Lloyd and Taylor, 1994).

$$\boldsymbol{R_{eco}} = \boldsymbol{R_{ref}} \cdot \boldsymbol{e}^{E_0\left(\frac{1}{T_{ref}-T_0}-\frac{1}{T_{air}-T_0}\right)} \tag{17}$$

Where R_{ref} (μmol·m−2·s−1) is the reference respiration rate at the reference temperature (T_{ref} = 15 °C), T_{air} is air temperature, T_0 is fixed at −46.02 °C, E_0 (°C) is the temperature sensitivity, a free parameter. A constant value is estimated for E_0 for the whole year, while R_{ref} is estimated every five days using a 15-day window (Reichstein et al., 2005).

Further references to NT estimations use the terms NT-GPP and NT-R_{eco}. The R code implementation for NT is available to download from https://github.com/bgctw/REddyProc (Wutzler et al., 2018).

2.4.2. Day-time partitioning method

Day-time (DT) partitioning differs from NT in that a light response curve (Lasslop et al., 2010) is parametrized using day-time measurements. NEE is estimated as follows:

$$\boldsymbol{NEE} = \frac{\boldsymbol{\alpha\beta R_g}}{\boldsymbol{\alpha R_g} + \boldsymbol{\beta}} + \boldsymbol{R_{eco}} \tag{18}$$

Where R_{eco} is a respiration model Eq. (17), R_g is the global radiation (Wm^{-2}), α ($\mu molCO_2 J^{-1}$) is the initial slope of the light response curve, and β ($\mu molm^{-2}s^{-1}$) is the maximum rate of CO_2 uptake of the canopy at light saturation. β is estimated using an exponentially decreasing function of atmospheric vapour pressure deficit of air (VPD):

$$\boldsymbol{\beta} = \begin{cases} \boldsymbol{\beta_0 e^{-k(VPD-VPD_0)}}, & VPD > VPD_0 \\ \boldsymbol{\beta_0}, & VPD < VPD_0 \end{cases} \tag{19}$$

Note that what is physiologically more relevant in β is the leaf-to-air VPD, which can vary from atmospheric VPD in the same direction as leaf temperatures vary from air temperature. However, flux sites measure atmospheric rather than leaf-to-air VPD.

The standard calibration procedure is done in two steps. First, E_0 and R_{ref} are estimated using night-time observations. The remaining parameters (α, β_0, k, and VPD_0) and R_{ref} (now using previous estimation as a prior) are fitted using Eq. (18) on day-time data. Night-time observations are periods with shortwave incoming radiation SW_{in} of <10 W m^{-2}, cross-checked against sunrise and sunset data derived from the local time and the potential radiation (Wutzler et al., 2018).

The acknowledged problem with this approach is that leaf respiration is reduced under light conditions compared to darkness (Pärnik and Keerberg, 1995; Hoefnagel et al., 1998). This light inhibition has been proposed as a source of mismatch between EC and independent R_{eco} measurements (Wohlfahrt et al., 2005; Wehr et al., 2016). A modified version of standard partitioning has been proposed to include this mechanism (Keenan et al., 2019). The modified DT version preserves the structure of the original DT but uses R_{ref} prior, fitted during night-time, for nocturnal partitioning while estimating daytime as usual. The R code implementation for DT's original and modified versions can be downloaded from https://github.com/bgctw/REddyProc (Wutzler et al., 2018). Unless specified otherwise, DT estimations follow the modified version (Keenan et al., 2019) and are referred to as DT-GPP and DT-R_{eco}.

2.4.3. A new wavelet-based, conditional sampling, model-free partitioning method

Direct observations of gross primary productivity (GPP) and ecosystem respiration (R_{eco}) are not feasible at the field scale, thus justifying the necessity of model-based partitioning. Thomas et al. (2008) and Scanlon et al. (2019) have proposed ingenious ways of incorporating assumptions on correlated processes between water vapour and CO_2 fluxes to compute new partitioning approaches of soil respiration (R_{soil}) and plant net primary productivity (NPP).

In this study, we take advantage of the wavelet time-frequency decomposition to go beyond what was proposed by Thomas et al. (2008) by proposing a discrete-wavelet-based conditional sampling, named hereafter DW-CS. With the empirical assumption that wavelet decomposition should be able to trap in each frequency the positive and negative "gusts" fluxes which are mixed up in the original signal, we conditionally sample the time-frequency decomposed products $\widetilde{wc}$ based on $\widetilde{wv}$ for each time-frequency point (t, j), where c and v stand for dry CO_2 and H_2O concentration mixing ratios (Fig. 3). This is a transposition of the quadrant decomposition of Thomas et al. (2008) from the (c',v') space into the ($\widetilde{wc}$, $\widetilde{wv}$) space. We get:

$$\widetilde{wc} = \widetilde{wc}^{+} + \widetilde{wc}^{-} = \underbrace{\widetilde{wc}^{+}|\widetilde{wv}^{+}}_{Q1} + \underbrace{\widetilde{wc}^{+}|\widetilde{wv}^{-}}_{Q2} + \underbrace{\widetilde{wc}^{-}|\widetilde{wv}^{-}}_{Q3} + \underbrace{\widetilde{wc}^{-}|\widetilde{wv}^{+}}_{Q3} \tag{20}$$

Where $Q1..4$ are the four quadrants ($\widetilde{wc}$, $\widetilde{wv}$) space, x^+ stands for sampling x when x is positive and the opposite for x^-, and $x|y$ stands for

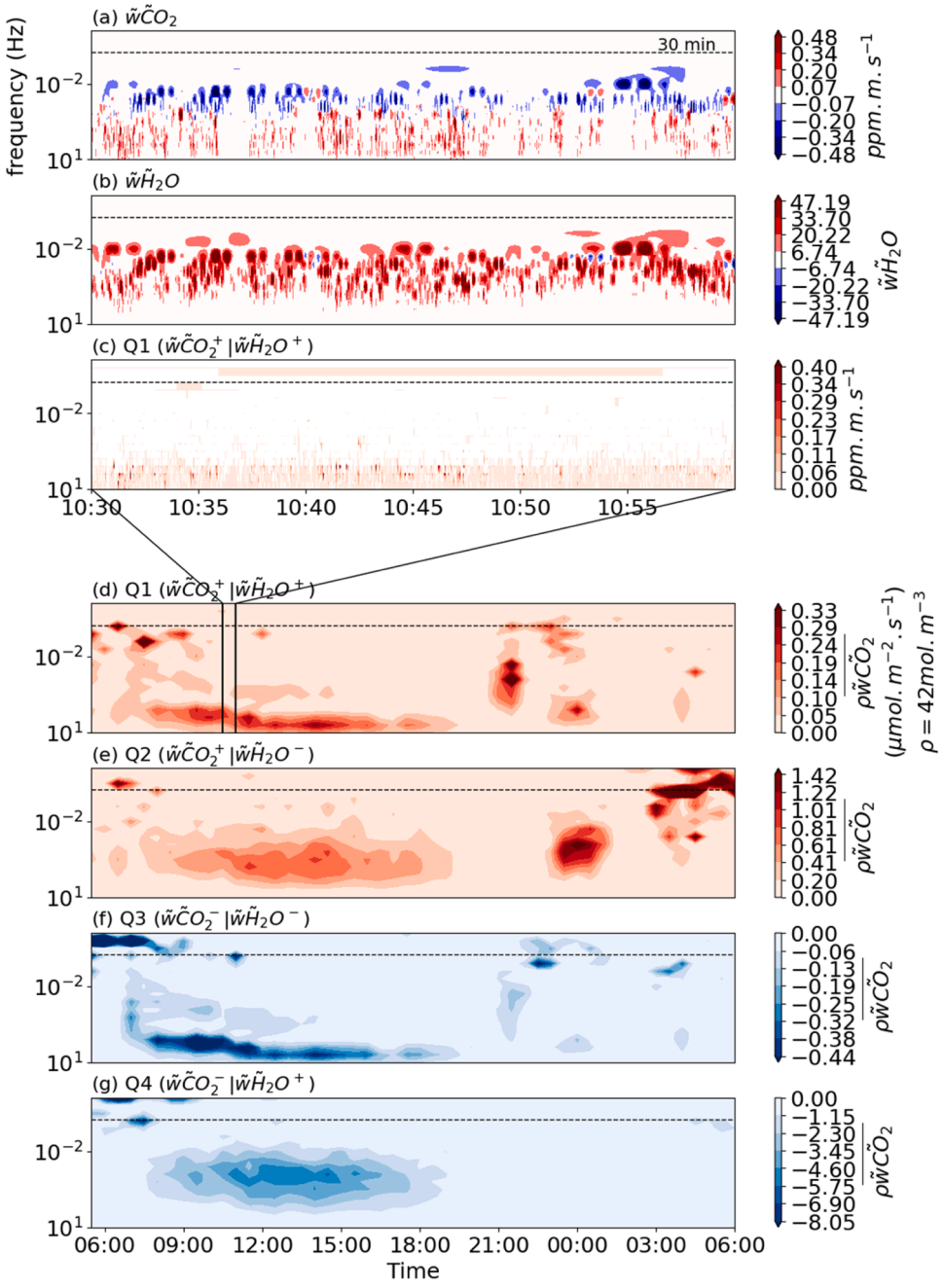

Fig. 3. (Cross-)scalogram for the quadrant analysis using the wavelet-based conditional sampling method. The black horizontal dashed line indicates the frequency equivalent to 30 min. Panels a-c show data at 20 Hz, and panels d-g show half-hourly averages. In panels d-g, the two black vertical lines indicate the data range in panels a-c. Note that scales are different. The data show is from FR-Gri, covering the period from May 13, 2022, 05:30 to May 14, 2022, 06:00.

sampling x when y is true.

Fig. 3 gives an illustration of the time-frequency decomposed product $\widetilde{wc}$, $\widetilde{wv}$, and their conditioned product $\widetilde{wc}^{+}|\widetilde{wv}^{+}$ (Q1), at 20 Hz over a 20 min period and the 30-minute covariance for the four quadrants corresponding to the right-hand side of Eq. (20) over a whole day. We note that the CO_2 uptake during the day is well-caught by the quadrant $\widetilde{wc}^{-}|\widetilde{wv}^{+}$ at frequencies around 0.1 Hz, while the day respiration, caught in the quadrant $\widetilde{wc}^{\mp}|\widetilde{wv}^{+}$, appears at frequencies higher than 0.1 Hz. The low-frequency flux (~30 min) observed in the very early morning, between 3 and 6 AM, in $\widetilde{wc}^{+}|\widetilde{wv}^{-}$ may be interpreted as respiration during dew formation. Similarly, this low-frequency flux later appears in $\widetilde{wc}^{-}|\widetilde{wv}^{-}$, potentially indicating photosynthesis occurring under light conditions but without sufficient energy to warm the surface.

In the following, we name the positive CO_2 fluxes $\widetilde{wc}^{+}$ as F^{+} and negative CO_2 fluxes $\widetilde{wc}^{-}$ as F^{-}. The physical meaning of $\widetilde{wc}^{+}$ and $\widetilde{wc}^{-}$ is the subject of discussion of this manuscript. However, we can say that $\widetilde{wc}^{-}$ is representative of events dominated by photosynthesis, while $\widetilde{wc}^{+}$ of events dominated by respiration. Taking advantage of photosynthesis' dependency on light, more precisely on photosynthetic photon flux density (PPFD), we forced F^{-} to zero during night (PPFD $\leq$ 10 μmol $m^{-2}\,s^{-1}$). We further considered that negative CO_2 fluxes conditioned by negative water vapour fluxes ($\widetilde{wc}^{-}|\widetilde{wv}^{-}$, quadrant Q3) had little physical meaning. Since a noise around 0 should average 0, we split the value of this quadrant in half and arbitrarily allocated it equally to F^{+} and F^{-} (see Fig. 4), which leads to the following definition of F^{+} and F^{-}:

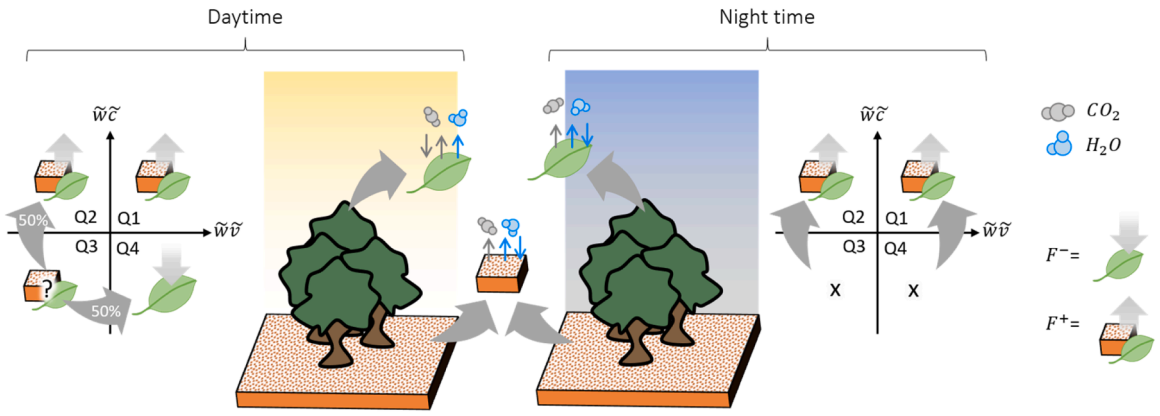

Fig. 4. Conceptual scheme for wavelet-based NEE flux partitioning. Quadrants and arrows in the figure show conceivable fluxes during day and night. In quadrants, grey arrows show reallocation from unlikable (question mark) and unreasonable ("x") fluxes towards the most probable actual flux.

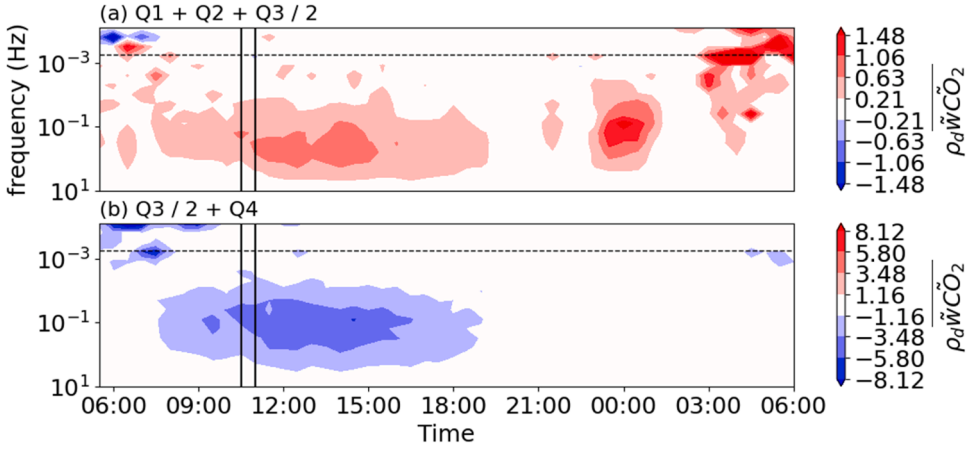

Fig. 5. Cross-scalogram of the partitioned fluxes using the wavelet-based conditional sampling method. The black horizontal dashed line indicates the frequency equivalent to 30 min. The two black vertical lines indicate the data range in panel a-c in Fig. 3. Note that scales are different for all figures. The data shown is from FR-Gri, covering the period from May 13, 2022, 05:30 to May 14, 2022, 06:00.

$$PPFD \leq 10\ \mu mol\ m^{-2}\ s^{-1} \begin{cases} F^+ = \widetilde{w'c'}^+ + \widetilde{w'c'}^- \\ F^- = 0 \end{cases}$$

$$\boldsymbol{PPFD} > 10\ \boldsymbol{\mu mol\ m^{-2}\ s^{-1}} \begin{cases} \boldsymbol{F^+ = \widetilde{w'c'}^+ + 0.5 \times \widetilde{w'c'}^- | \widetilde{w'v'}^-} \\ \boldsymbol{F^- = \widetilde{w'c'}^- | \widetilde{w'v'}^+ + 0.5 \times \widetilde{w'c'}^- | \widetilde{w'v'}^-} \end{cases} \quad (21)$$

Fig. 5 illustrates the 30-minute cross-scalogram for F^+ and F^- before all nocturnal flux is moved to F^+. Note that nocturnal F^- is, in any case, very small and mainly comes from Q3.

2.5. Performance measurements

Comparisons between methods were carried out using mean bias and the annual gap-filled CO2 flux balance error. Defined as:

$$\boldsymbol{Mean\ Error\ (bias)} = \frac{1}{\boldsymbol{N}} \sum_{n=1}^{N} \left(\boldsymbol{NEE_{x,n} - NEE_{y,n}}\right) \quad (22)$$

$$\boldsymbol{Mean\ Absolute\ Error} = \frac{1}{\boldsymbol{N}} \sum_{n=1}^{N} \left|\boldsymbol{NEE_{x,n} - NEE_{y,n}}\right| \quad (23)$$

Where N equals the amount of data, $NEE_{x,n}$ is the Net Ecosystem Exchange calculated using one of the x methods among EC_S and DW-EC at a time n.

3. Results

3.1. Comparison of the CO_2 flux computed by EC and by DW-EC

The initial step of the partitioning method involves calculating the net flux using wavelet transform; here, we compare CO_2 flux (Net Ecosystem Exchange, NEE) derived from EC_S and DW-EC methods to ensure the DW-EC gives similar results as the EC_S. During the photosynthetically active months (warmer months for FR-Fon and crop seasons for FR-Gri), the two sites were carbon sinks with a negative NEE (Fig. 6). NEE flux ranged from −10 to 6 μmol m^{-2} s^{-1}, with stronger respiration during winter and spring at the crop site compared to the forest site. Daily mean NEE estimated by EC_S and DW-EC were very close to each other, with R^2 above 0.97, mean errors of 0.1 and 0.05 μmol m-2 s-1 and absolute error of 0.33 and 0.38 μmol m-2 s-1 for FR-Fon and FR-Gri, respectively. Standard EC yielded 8 and 12 % larger fluxes than wavelet-based EC for FR-Fon and FR-Gri.

During winter, when the trees have lost their leaves and crop sites are bare soil, the decrease in photosynthesis transforms sites into sources with a positive NEE. As a consequence, NEE in FR-Fon showed an annual seasonality, while FR-Gri showed a pattern consistent with the crop cycles. We observe a substantial decrease in absolute value in the NEE for short periods during summers and springs for all years. Some relate to cloudy days, others to high vapour pressure deficit, and in June and July 2019, France was hit by short heat waves (Sousa et al., 2020; Pohl et al., 2023). In the crop site (FR-Gri), we identify the crop season in the

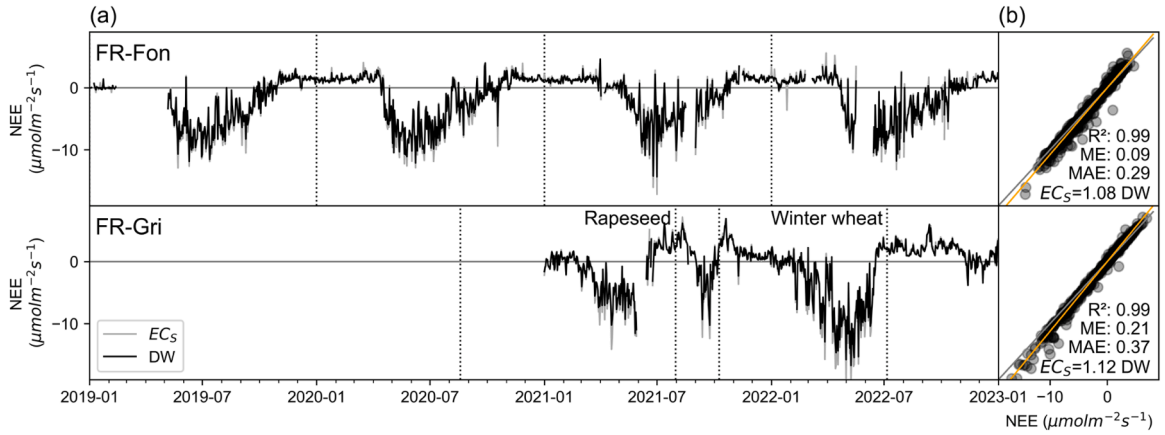

Fig. 6. Daily average CO_2 flux computed using wavelet-based (black, DW) and standard EC (grey, EC_S). Time series are shown in (a), while (b) shows ECs against DW-EC. The fluxes were not gap-filled.

spring of both years and the intercrop in Autumn 2021 by the decrease in NEE. The harvest is done after senescence when NEE has already shown positive values. Finally, the crop site exhibited earlier growth than the forest site, as expected due to species-specific differences in phenological responses. Trees generally require different environmental cues, such as specific temperature thresholds or photoperiod conditions, to initiate foliar development, resulting in a later onset of growth compared to winter crops, which begin their growth phase earlier in the year.

A good match is also observed for diel and seasonal patterns: both methods show clear and expected patterns for NEE for these ecosystems (Fig. 7). In the forest site, during March and April, we can see peaks in the EC_S-NEE 5th and 95th percentiles, which are lower in DW. These two months had the highest non-stationarity in the site, yielding 60 % of the observations unreliable. These peaks may be due to early morning emissions from the release of accumulated gases as turbulence develops. The same EC_S-NEE peaks are seen for the crop site but are not systematically related to the stationarity flag and occur more often. These spikes happen more often at night and may be related to advection. A windrose analysis does not show a preferential wind direction.

The half-hourly DW- and EC_S-NEE data agreed well when both were high-quality data, with an R^2 of 0.98, while medium-quality data showed an R^2 of below 0.72, and low-quality data showed an R^2 below 0.3. High-quality data showed limited errors on NEE (mean error below 0.2 μmol m^{-2} s^{-1} and mean absolute error (MAE) 0.6 μmol m^{-2} s^{-1}), while medium and low-quality data showed MAE up to 2.6 μmol m^{-2} s^{-1} ().

3.2. *Example of time-frequency domain representation of the CO_2 fluxes*

Wavelet-based fluxes, calculated in both frequency and time domains, allow visualization of CO_2 flux dynamics across both dimensions, as illustrated in the cross-scalograms presented in Fig. 8 and Fig. 9 over late spring and late fall weekly periods in 2022.

Fig. 8 shows that both sites share a clear daily pattern of daylight carbon sequestration and nocturnal emissions. The NEE co-spectra

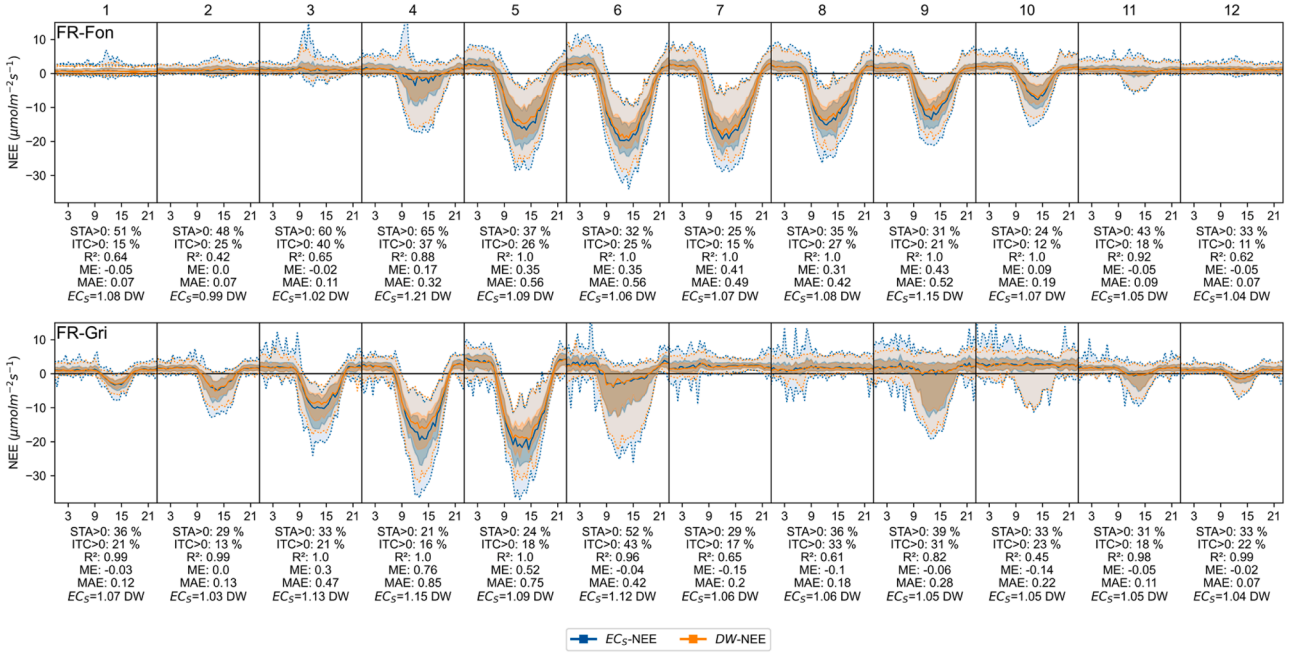

Fig. 7. Half-hourly NEE estimated monthly using EC_S (blue) and DW (orange). The darker region indicates interquartile (25th and 75th percentile), and the lighter region with dotted lines indicates the 5th and 95th percentile. Below the curves, the monthly statistics are shown: the percentage of non-stationarity (STA>0) and low turbulence (ITC>0) data, the correlation coefficient (R^2), the mean error (ME, μmol m−2 s−1), the mean absolute error (MAE, μmol m−2 s−1) and the linear fit.

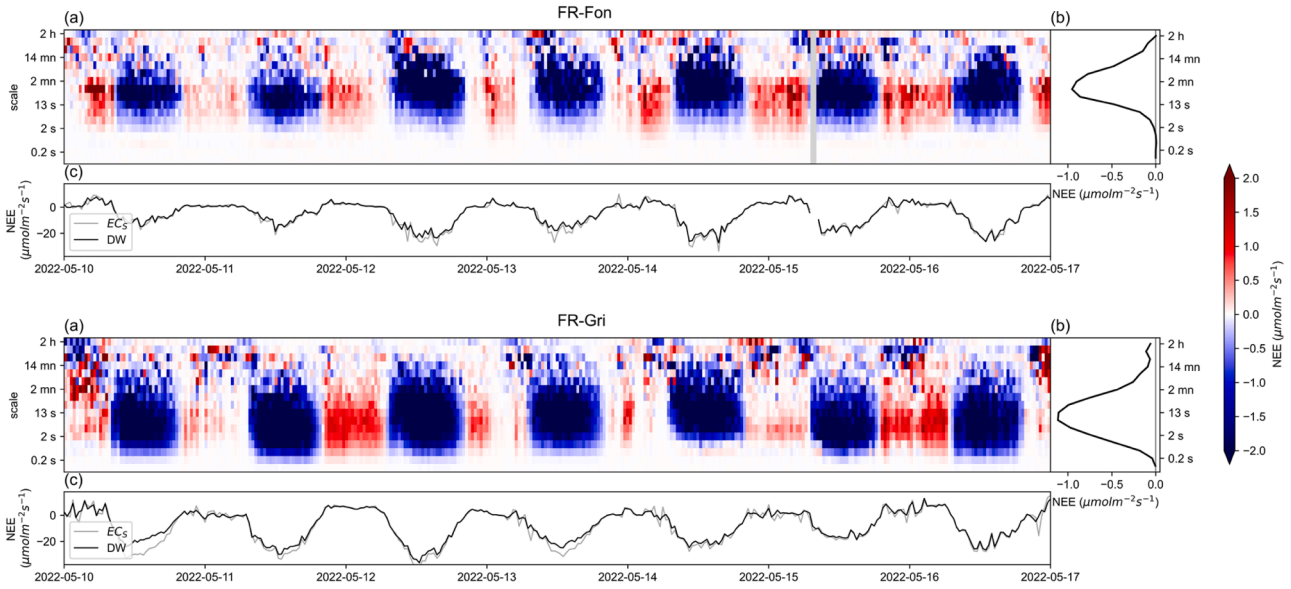

Fig. 8. CO_2 flux and co-spectra during a late-spring week. (a) NEE time-frequency decomposition was derived by DW-EC and averaged every half-hour. Colours indicate NEE, and grey indicates missing data. (b) NEE co-spectra over the period computed from the time-frequency decomposition of (a) averaged over time. (c) Daily average NEE computed from the NEE time-frequency decomposition integrated over scales up to 30 min (DW, black) and the standard EC method (EC_S, grey).

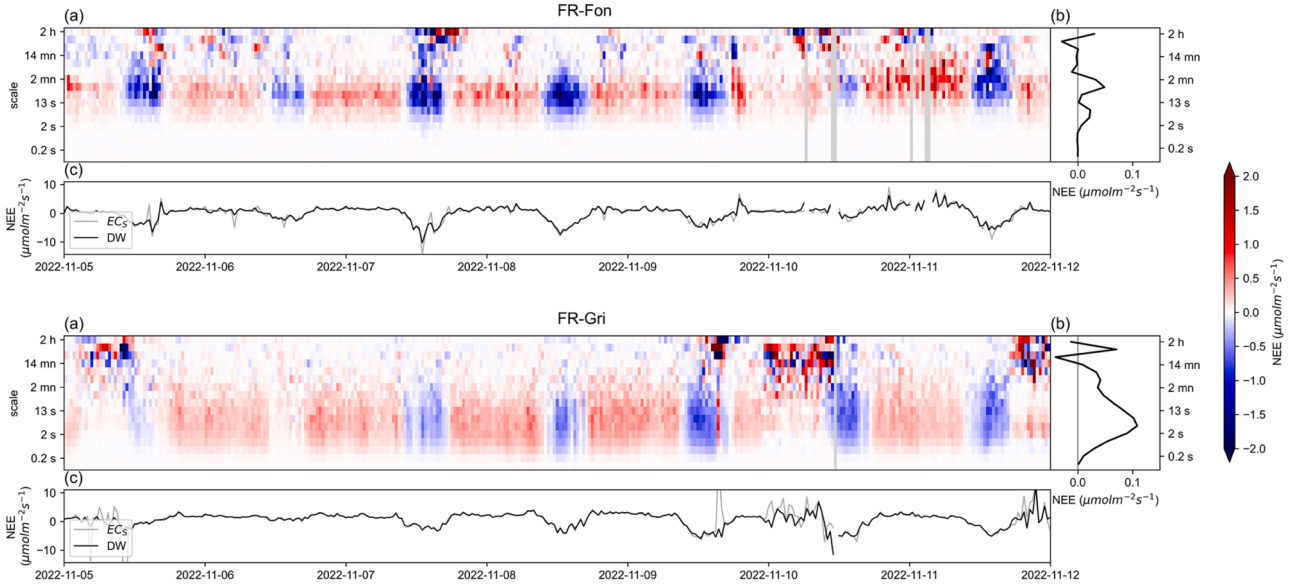

Fig. 9. Same as Fig. 8 but for a late-fall week.

(Fig. 8.b) shows little information on scales below 2 s (frequencies higher than 0.5 Hz) for FR-Fon and below 0.2 s ($f > 5$ Hz) for FR-Gri. The difference is expected as the spectrum depends on height, with smaller eddies contributing more to the flux in shorter towers than taller ones (Kaimal and Finnigan, 1994).

Fig. 9 shows a lowering of the flux amplitude during colder months, varying between −10 and 5 μmol m^{-2} s^{-1} compared to warmer months (Fig. 8). During this period, in FR-Fon, leaves have fallen, and FR-Gri has only very small barley plants and mostly bare soil.

3.3. Co-spectral characteristics of partitioned CO_2 fluxes across seasons and stability

In Fig. 10, the co-spectrum profile for the net flux (the same as in Fig. 8 and Fig. 9) shows differences when compared to the positive ($\widetilde{wc}^{+}$) and negative ($\widetilde{wc}^{-}$) components of the flux. The frequency profiles for $\widetilde{wc}^{+}$ and $\widetilde{wc}^{-}$ were distinct during . late-Spring (Fig. 10.a and c) but similar during late-Fall (Fig. 10.b and d).

During a late-spring week, when fluxes were relatively high for both sites, the high frequency contributed more to the flux in $\widetilde{wc}^{-}$ than in $\widetilde{wc}^{+}$. For FR-Fon, there is a drop in contribution from frequencies lower than 50 s (0.02 Hz), and in FR-Gri, a decrease in contribution can be seen for frequencies lower than 6 s (0.16 Hz). The higher contribution of lower frequencies on the negative part of the CO_2 flux suggests large coherent structures may, on average, contribute more to the NEE, which is mostly negative during the spring, than to the soil respiration, which is positive. During a late-fall week, the profiles were very similar, with fluxes close to zero, yielding a poorly defined co-spectrum for both sites.

During stable conditions (primarily at night; Figure 11. b, d) and less active months (Fig. 10.b, d), the co-spectral profiles of F^{+} and F^{-} (or

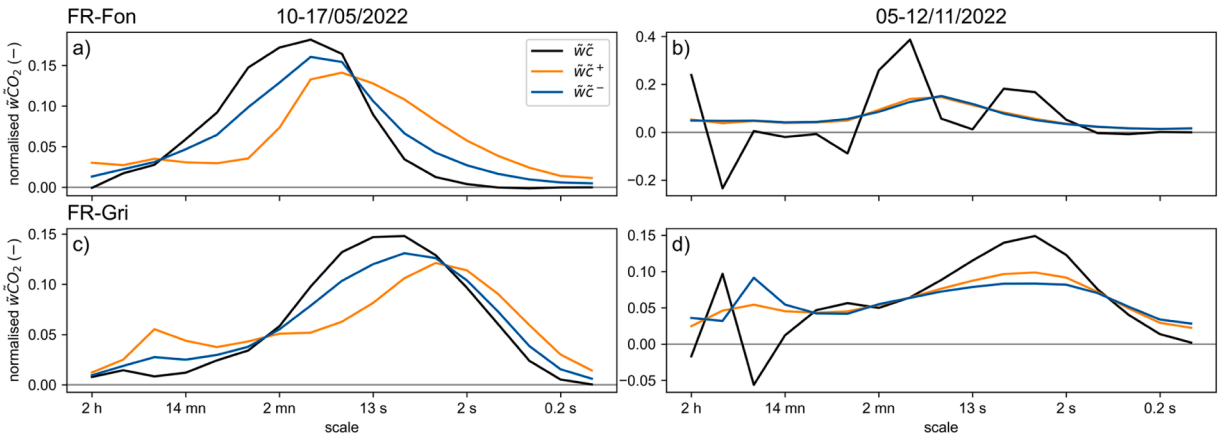

Fig. 10. Mean CO_2 flux in frequency during a late-spring (a, c) and late-fall (b, d) week for $\widetilde{wc}$ and its positive and negative components. The same data is used in Fig. 8 and Fig. 9 for FR-Fon (a, b) and FR-Gri (c, d).

$\widetilde{wc}^+$ and $\widetilde{wc}^-$) become similar with a nearly identical peak. This similarity happens when minimal or no photosynthetic activity is expected, whereas differences in profiles suggest the presence of distinct simultaneous processes. This finding underscores a key limitation of the method when using atmospheric gases such as CO_2 and H_2O as tracers. Since these gases are abundant in the atmosphere, conditional sampling produces small but nonzero partitioned fluxes. For the same reason, the quadrant Q3 is not considered an interpretable flux and is instead arbitrarily divided into F^+ and F^-.

3.4. Comparison of the new DW-CS method with well-established flux partitioning methods

In this section, we compare the partitioned fluxes using the new DW-CS method and, based on the quadrant analysis of $\widetilde{wc}$ and $\widetilde{wv}$, F^+ and F^-, with R_{eco} and GPP from the well-established nighttime (NT) and daytime (DT) methods. We used DW-NEE as input for the NT and DT partitioning methods to evaluate only the partitioning methods since we observed some differences between DW-NEE and EC_S-NEE. Overall, the partitioning methods agreed well over daily periods (Fig. 12b and c). In particular, the NT to DW-CS comparison (Fig. 12.c) shows a mean absolute daily error (0.81 μmol m^{-2} s^{-1} in FR-Fon and 0.65 μmol m^{-2} s^{-1} in FR-Gri) lower than the random uncertainty of the net flux (1.03 μmol m^{-2} s^{-1} in FR-Fon and 0.73 μmol m^{-2} s^{-1} in FR-Gri). The NT method compared better with DW-CS than the DT method, with an MAE between DT and DW-CS larger by 0.25 to 0.35 μmol m-2 s-1 than the NT and DW-CS.

Beyond differences in mean values, we notice that the DW-CS partitioning method notably avoids the occurrence of unphysical pulses in GPP and Reco, in contrast to both NT and DT. In particular, DT exhibits several brief but intense spikes in GPP and Reco, which appear to coincide with fluctuations in daily weather conditions. During the summer of 2019, the DT Reco spikes corresponded to observed heat waves. These overestimations of GPP and Reco by DT are likely due to the methodology that can not deal with extreme temperatures or precipitations. NT yielded erroneously positive GPP at the crop site in August, after harvest, in October 2021, after harvest and herbicides application, and in July 2022, after application of solid manure and barley seeding. These management events generate transitory R_{eco} fluxes, which cannot be easily handled by the NT or the DT methods based on a multiple-day window period. Furthermore, respiration during these events would originate from the upper soil surface and respond more closely to surface temperatures than deeper soil temperatures, which the DT and NT methods would not capture. On the contrary, the DW-CS partitioning method has the comparative advantage of being free of any calibration window.

GPP diel pattern agreed quite well between the DW-CS and the standard NT and DT methods (Fig. 13). On the contrary, the R_{eco} diel patterns differed significantly. As expected from the standard methods equations, NT-R_{eco} followed a daily temperature cycle, increasing smoothly with temperature across seasons. DT-Reco values were generally higher and showed an abrupt step increase just before sunrise, corresponding to the model's transition between night and day. This likely reflects the onset of modelled GPP at dawn, while measured fluxes reflect the release of nocturnal storage. The DW-CS- R_{eco} pattern was more complex: it remained relatively flat at night, dipped around sunrise and sunset and displayed an inverted U-shape during the daytime. During spring/peak season, DW estimated R_{eco} was larger during the day than at night, especially at the crop site, while the opposite was observed during senescence/summer.

3.5. Diel patterns of conditional fluxes and their association with soil and plant respiration

A closer inspection of the $\widetilde{wc}$ fluxes conditioned by $\widetilde{wv}$ (Figure 14) reveals diel pattern resemblance between $\widetilde{wc}^+|\widetilde{wv}^+$ and soil respiration (R_{soil}) (daytime decrease during certain seasons), and $\widetilde{wc}^+|\widetilde{wv}^-$ and plant respiration (R_{plant}) (bimodal, with a maximum during daytime) as found in Järveoja et al. (2020). R_{soil} is expected to respond to soil temperature rather than air temperature, so follow the soil's delayed warming and cooling pattern at the depth where respiration is maximum. We found here that $\widetilde{wc}^+|\widetilde{wv}^+$ diel pattern follows soil temperature at 16 cm depth for FR-Fon and 30 cm in FR-Gri (differences relate to available measurement depths) while $\widetilde{wc}^+|\widetilde{wv}^-$ follows rather closely air temperature and incoming radiation, suggesting indeed that $\widetilde{wc}^+|\widetilde{wv}^+$ may represent soil respiration and $\widetilde{wc}^+|\widetilde{wv}^-$ plant respiration. This interpretation is consistent with the dual-source respiration model proposed by Wohlfahrt and Galvagno (2017), who emphasized that ecosystem respiration arises from distinct above- and below-ground sources driven by different temperature regimes. They showed that phase shifts between air and soil temperatures induce a hysteresis in respiration–temperature relationships, cautioning against using a single temperature as a driver.

4. Discussion

4.1. Co-spectral characteristics of NEE and the partitioning into positive and negative fluxes

The higher measurement height at FR-Fon led to an expected and observed shift of the co-spectra to lower frequencies than FR-Gri (Fig. 10.a and c). Moreover, the co-spectra of the negative flux component $\widetilde{wc}^-$ exhibited a lower frequency contribution than the positive

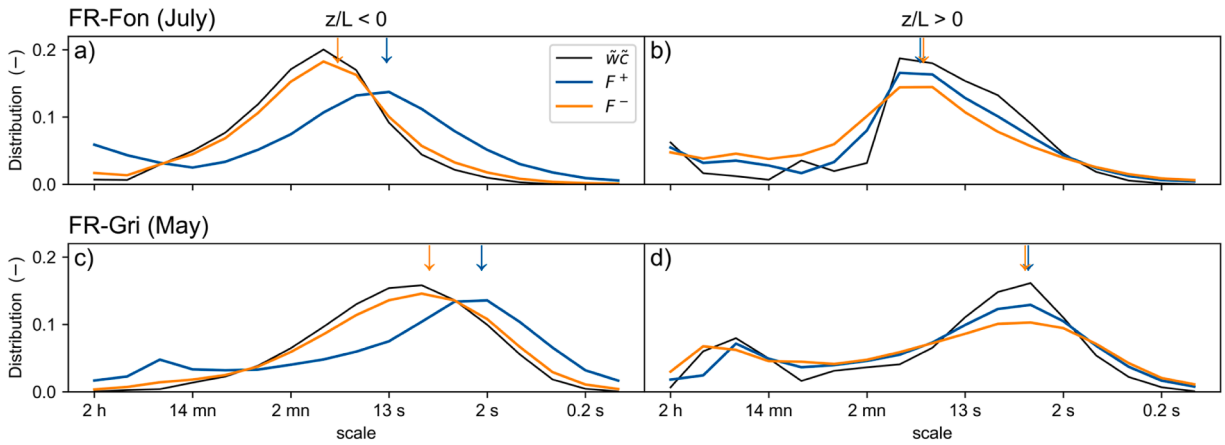

Fig. 11. Mean co-spectra of $\widetilde{wc}$, along with F⁺ and F⁻ partitioned fluxes. Data is grouped by neutral and unstable conditions (z/L < 0, a, c) and stable (z/L > 0, b, d) conditions. The period corresponds to the peak ecosystem activity in 2022: July for FR-fon and May for FR-Gri. Co-spectra curves are normalized to sum to 1. Arrows indicate the scale with maximum values. Monthly results are provided in .

component $\widetilde{w}\widetilde{c}^{+}$. These results are confirmed in Fig. 11.a and c which show the partitioned fluxes (F^+ and F^-) during months with high carbon sequestration (in July for FR-Fon and May for FR-Gri).

These findings are consistent with Thomas et al. (2008), who found that 60 % of respiration events were associated with small-scale eddies (timescales shorter than 0.1–0.05 s), and Scanlon and Albertson (2001), who showed that high-frequency eddies transport CO_2-enriched air from below the canopy.

The transport path can explain the observed differences in the co-spectra profile: eddies moving from the canopy top, poor in CO_2, versus those coming from the soil, rich in CO_2. Vegetation affects turbulence through sweep and ejection events (Zhu et al., 2007; Poggi et al., 2004). The transport through the canopy causes eddies to break down into smaller structures along the Kolmogorov cascade as they encounter leaves, stems and branches.

We hypothesise that these spectral profile differences would diminish in flatter ecosystems (e.g., grasslands) compared to layered structures (e.g., forests). Further investigation is needed to determine whether partitioning produces equally defensible fluxes across different canopy structures.

4.2. On conceptual framework around F^- and F^+

Our results compared F^- with estimated GPP and F^+ to estimated R_{eco}. We acknowledge that these estimates are subject to conceptual and methodological limitations. Notably, the GPP estimate from the NT method aligns more closely with 'apparent photosynthesis' (encompassing both carboxylation and photorespiration) rather than 'true photosynthesis,' which considers only carboxylation. This discrepancy arises because of the extrapolation from nighttime respiration measurements to daytime conditions without adequately accounting for photorespiration and the suppression of mitochondrial respiration in light. Conceptually, F^- is more closely aligned with net photosynthesis, encompassing carboxylation, photorespiration, and dark respiration. However, given the current state of the method, its interpretation is likely valid only under conditions where carboxylation dominates, i.e., when net photosynthesis represents a carbon sink, since only then does the quadrant framework capture the negative relation between CO_2 and water fluxes. Here, we do not differentiate any further between net, apparent and true photosynthesis and refer readers to Wohlfahrt and Gu (2015) for a comprehensive discussion of these distinctions and their implications.

Further clarification is warranted regarding the interpretation of F^+ with R_{eco}, as F^+ includes $\widetilde{wc}^{+}|\widetilde{wv}^{+}$ (Q1) and $\widetilde{wc}^{+}|\widetilde{wv}^{-}$ (Q2). While Q1 is conceptually straightforward, respiration is a source of CO_2 and H_2O, and Q2 requires additional interpretation. Although daytime water vapour fluxes are typically positive due to evaporation and transpiration, transient negative excursions can occur from turbulent mixing or the entrainment of drier air from above the canopy under strong convective conditions. When the ejection of these incursions coincides with the upward transport of CO_2 from ecosystem respiration, the resulting events fall into Q2, characterized by a positive CO_2 flux and negative water vapour flux. This association becomes more intuitive at night, as condensation leads to net negative water vapour fluxes that frequently coincide with CO_2 release from respiration. These patterns explain the quadrant analysis without necessarily indicating a physiological coupling between water vapour and CO_2 exchange. These patterns may also help explain why Q2 events, associated with large-scale entrainment and ejection processes, tend to occur at lower frequencies than Q1 during the day (Fig. 3) and why, at night, Q2 activity, potentially driven by condensation, emerges more prominently during the latter part of the nocturnal period, when the soil temperature starts to fall (Fig. 14).

4.3. On the comparison between the standard and the new partitioning methods and their uncertainties

Results show a good comparison from daily mean partitioned fluxes (Fig. 12). The ratios between the nighttime and DW-CS methods estimations are closer during periods with large fluxes (). Differences between methods are more pronounced at FR-Fon during the leafy season, where DW-CS estimates are lower than NT. This difference is consistent with the interpretation of F^- as canopy net photosynthesis, which includes R_{leaf}. The hypothesis that F^- represents canopy net photosynthesis is supported by spectral analysis, which indicates transport by larger eddies. This spectral profile is consistent with fluxes originating from the top of the canopy, with fewer obstacles. Consequently, F^+ is interpreted to represent below-canopy fluxes, therefore including heterotrophic and root respiration. It is possible that it includes part of the below canopy net photosynthesis from low vegetation after periods of decoupling.

It is difficult to go beyond these qualitative considerations and estimate more precisely the part of GPP and Reco captured by F^- and F^+. Moreover, these ratios likely vary depending on canopy type, 3D structure, height, leaf area, and vertical leaf area distribution as reported for the Thomas et al. (2008) method (Klosterhalfen et al., 2019a), as well as any other factors that influence aerodynamic roughness. A promising avenue for numerical validation could involve large-eddy simulation (c. f. Zahn et al., 2024).

Although often simplified into single, aggregated GPP and R_{eco} fluxes

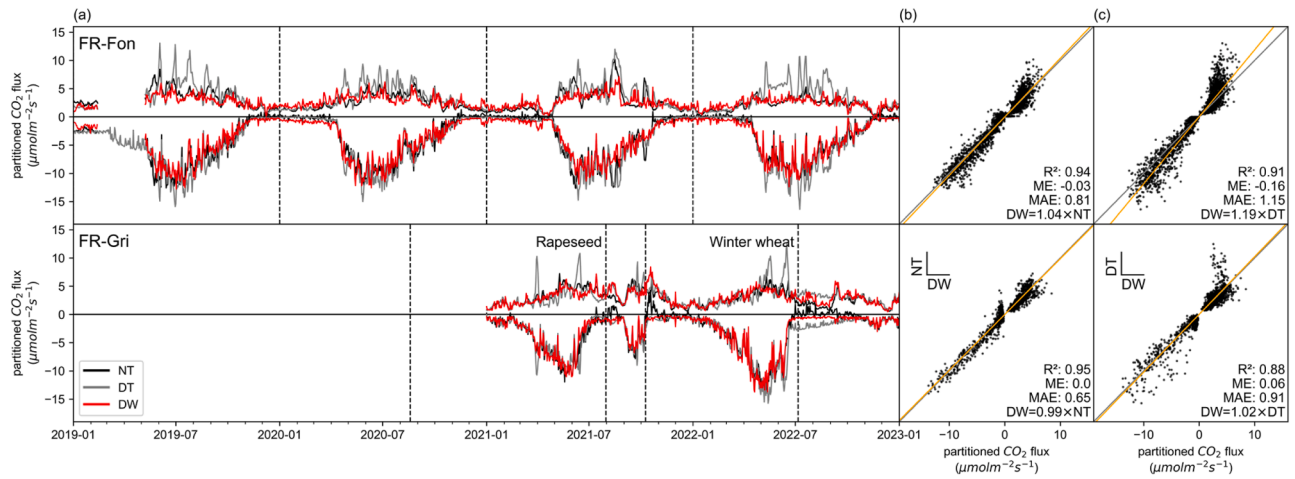

Fig. 12. (a) Daily averaged CO_2 partitioned fluxes. GPP and R_{eco} were calculated using commonly used nigh-time (NT, black) and day-time (DT, grey) partitioning methods and F^- and F^+ were calculated using wavelet-based direct DW-CS (DW, red) partitioning methods, all using DW-NEE as base data. Positive values show R_{eco}, and negative values show GPP. Dotted vertical lines show the start or end of the season (calendar years for forest site FR-Fon and cropping season for FR-Gri). (b) Daily NT versus DW GPP and R_{eco} (both on the same graph), in grey 1:1, in orange linear fit. On the bottom, statistics for GPP and R_{eco} combined the correlation coefficient (R^2), the mean error (ME, μmol m^{-2} s^{-1}), the mean absolute error (MAE, μmol m^{-2} s^{-1}) and the linear fit. (c) same as (b) for DT versus DW comparison.

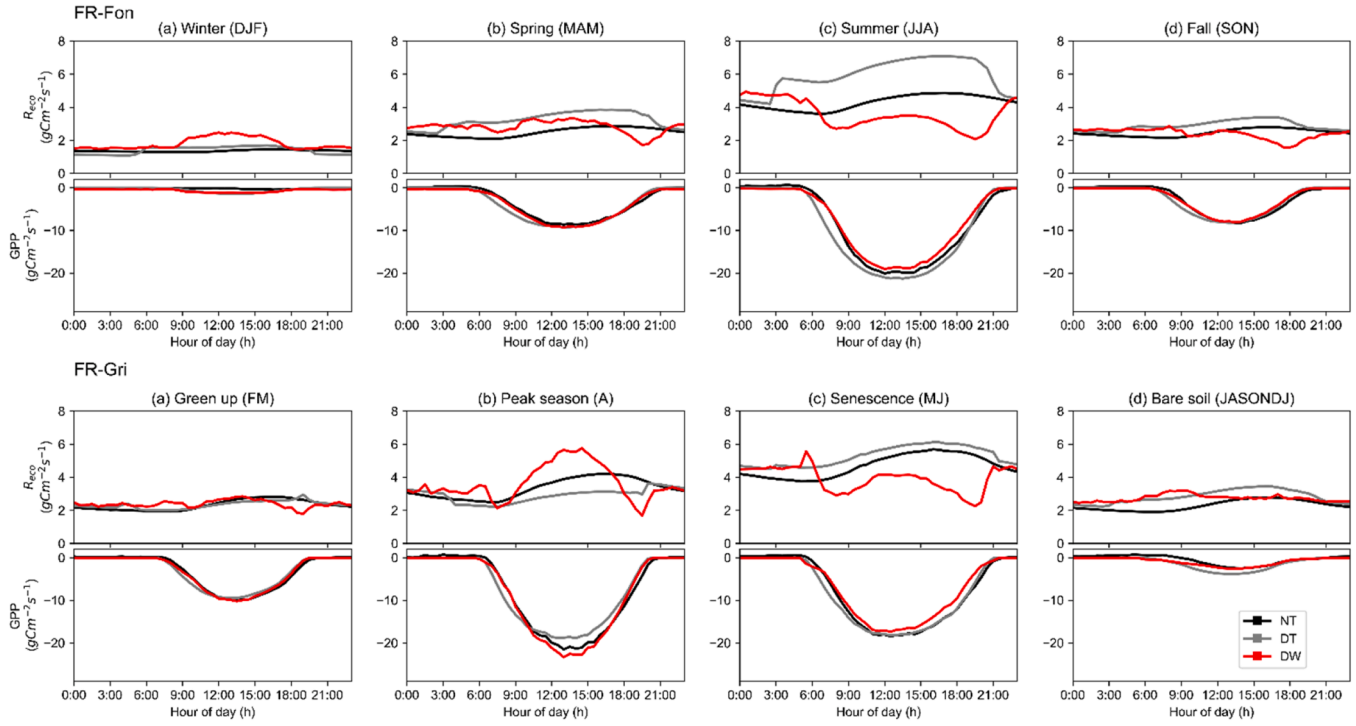

Fig. 13. Diel patterns of R_{eco} and GPP estimated calculated using commonly used nigh-time (NT, black), day-time (DT, grey) and wavelet-based direct DW-CS (DW, red) partitioning methods during climatic seasons (for FR-Fon) and the phenophases (for FR-Gri) of green-up, peak season, senescence, and bare soil (excluding September 2021 due to intermediate crop). Months are indicated by their first letter in parentheses. Note that R_{eco} and GPP are not on the same scale. Monthly results in .

and estimated using a single temperature driver for all respiration processes, ecosystem carbon dynamics are far more complex (Fig. 15). Ecosystem fluxes arise from multiple sources and canopy layers, each responding differently to environmental conditions. This complexity becomes particularly evident in the DW-CS F^* signal, which captures diel variations in R_{eco} and reveals a bimodal pattern (Fig. 13), consistent with chamber-based (Järveoja et al., 2020) and isotopic partitioning (Wehr et al., 2016) studies. These patterns are attributed by Wehr et al. (2016) to the inhibition of leaf respiration in light and by Järveoja et al. (2020) to the differential response of R_{eco} to soil temperature and air or plant temperature. Our results resonate with the dual-source respiration framework (Wohlfahrt and Galvagno, 2017), emphasizing the need to distinguish temperature drivers linked to specific ecosystem components.

Another interesting finding (Fig. 13) is that during the crop's peak growing season, DW-CS F^+ is significantly higher than NT R_{eco} during daytime. This increase likely reflects increased autotrophic respiration concomitant with high GPP, a feature missed by the NT method, which uses nocturnal calibration but is theoretically capturable by DT. This, however, was not observed. Strangely, DT's highest GPP in FR-Gri was

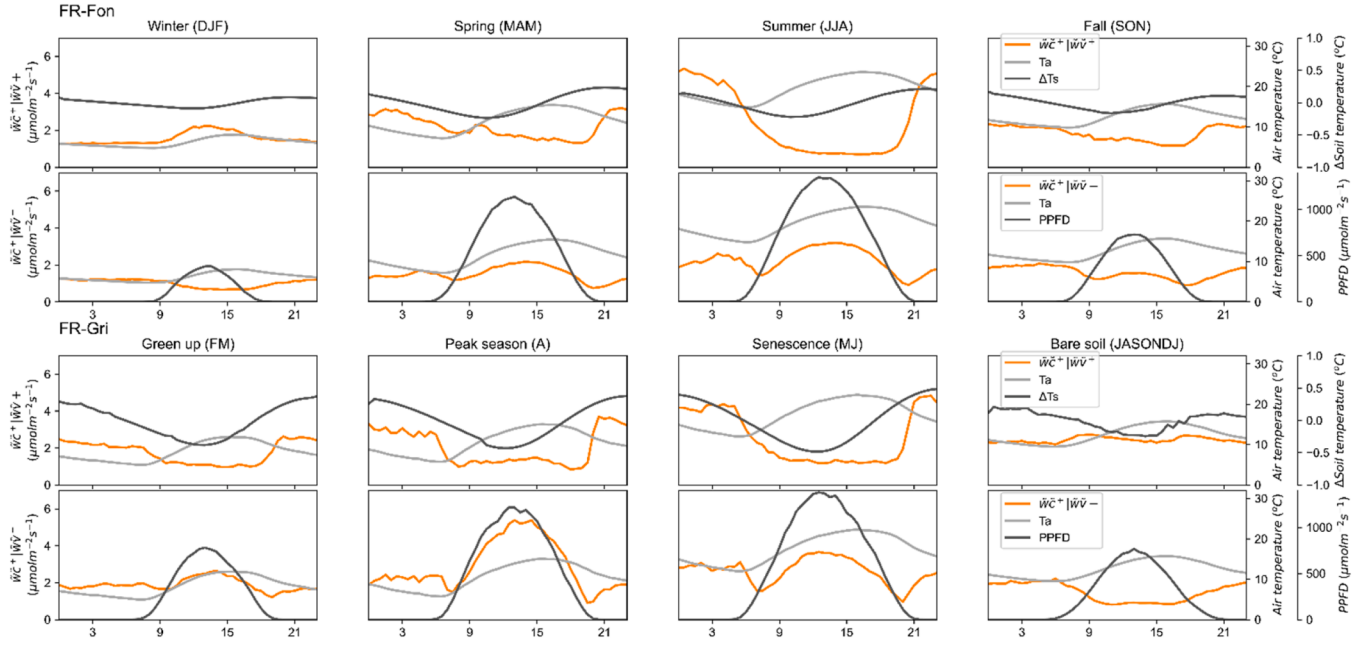

Fig. 14. Diel patterns of $\widetilde{wc}^{+}|\widetilde{wv}^{+}$ (associated to heterotrophic respiration, Rh) and $\widetilde{wc}^{+}|\widetilde{wv}^{-}$ (associated to autotrophic respiration, Ra) and Rh's and Ra's main abiotic controls including air temperature (T_{air}), soil temperature at 16 cm depth in FR-Fon and 30 cm in FR-Gri (ΔT_{soil}, showed as deviation from the seasonal mean for readability), and photosynthetic photon flux density (PPFD) during climatic seasons (FR-Fon) and the phenophases of green-up, peak season, senescence, and bare soil, months indicated in parentheses. (cf. Järveoja et al., 2020, Fig. 4).

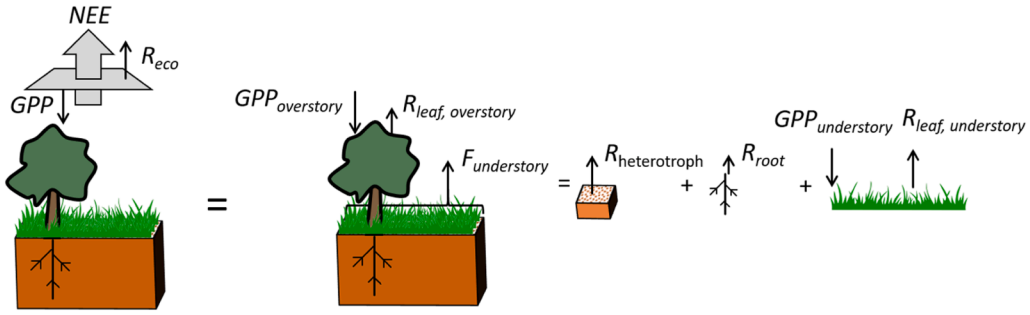

Fig. 15. A simplified scheme of ecosystem fluxes containing Gross Primary Production (GPP) ecosystem respiration (R_{eco}). The diagram differentiates between overstory and understory components and separates respiration into its key sources: leaf (R_{leaf}), root (R_{root}), and heterotrophic respiration ($R_{heterotroph}$). Note that $R_{eco} = R_{leaf} + R_{root} + R_{heterotroph}$.

during senescence, when the weather was warmer, but biologically, the plant was not productive anymore.

Thus, a better physiological understanding, supported by independent methods like understory EC, chambers, isotopic tracers (e.g., $^{13}CO_2$), COS, or VOCs, is necessary to characterize the processes isolated by DW-CS partitioning.

4.4. On the differences and perspectives of wavelet-based eddy covariance compared to conventional method

Unlike traditional EC methods, wavelet analysis does not require stationarity (e.g., Torrence and Compo, 1998; Mauder et al., 2007). Our results show that this represents around 10 % more high-quality data when using DW-EC. Typically this could decrease short gaps, improve gap-filling (Moffat et al., 2007; Lucas-Moffat et al., 2022) and limit bias related to their filling (Du et al., 2014; Vekuri et al., 2023) for CO_2, as well as for typically non-stationary surface fluxes like CH_4 and N_2O (Irvin et al., 2021; Mishurov and Kiely, 2011). A potential criticism is whether fluxes calculated during non-stationary events are truly interpretable. Addressing this concern first requires developing a solution for stationarity testing, as conventional methods are not well-suited to these conditions.

The stationarity test (STA, Eq. (13)) relies on $\overline{w}$ and $\overline{c}$ differing over 5-minute and 30-minute intervals. In such cases, the fluctuations w' and c', based on $\overline{w}$ and $\overline{c}$, would also be distinct. If instead of w' and c' we use $\widetilde{w}$ and $\widetilde{c}$, the STA test will yield zero as the covariance is computed on a detrended series, which remains unchanged, i.e. detrending is performed independently of correlation calculation (local flux estimations, see Eqs. (9) and (10)). By reformulating Eq. (13) to explicit time and frequency, we find a new test which is roughly equivalent to comparing the integral of the co-spectrum over the frequency range of 5 to 30 min with the integral of the 30-minute co-spectrum (supplementary material section A). Applying the new test was beyond the scope of this study but highlights a gap in developing a fully wavelet-based EC processing chain.

Regarding CO_2 flux estimations, wavelet decomposition generally underestimates fluxes by 8–12 % compared to EC, likely due to the detrending nature of wavelet transforms. We know detrending can lead to 2–15 % flux underestimations if not corrected (Rannik and Vesala, 1999). While low-frequency corrections may reduce this discrepancy,

they must be applied cautiously to avoid distorting the signal. Furthermore, careful consideration of preprocessing corrections is necessary. For instance, time lag and axis rotation can introduce artificial breaks in the data. However, frequency-dependent time lags could be helpful for sticky compounds like ammonia or VOCs to account for time and phase shifts (Ferrara et al., 2012). Wavelet analysis may require new technical developments but could offer improvements over standard EC methods.

4.5. Perspectives for direct partitioning using a multi-tracer approach

The conditional sampling method presented here could be further expanded by incorporating tracers that differentiate between ecosystem sources, such as soil versus plant or heterotrophic versus autotrophic processes. Carbonyl sulphide (COS), a proxy for photosynthesis (Maseyk et al., 2014), combined with CO_2 and H_2O fluxes, offers a promising route toward finer partitioning of ecosystem fluxes. Similarly, methanol emissions, measurable by EC (Loubet et al., 2022), could help differentiate soil and plant fluxes (Voyard et al., 2024). In other contexts, carbon monoxide has served as a tracer for fossil fuel emissions (Super et al., 2017). These more precise tracers may be markers of eddies carrying process signatures, identifiable in both time and frequency domains. One avenue forward could involve distinguishing flux regimes based on species co-variation: canopy-driven fluxes marked by CO_2 uptake, H_2O release, near-zero CO flux, and anthropogenic fluxes characterized by concurrent CO_2 and CO release. The remaining should contain sub-canopy fluxes, mainly soil respiration but potentially some residual net low vegetation photosynthesis.

Applying wavelet-based conditional sampling to multi-species datasets could enhance our ability to resolve ecosystem carbon dynamics, overcoming the limitations of single-variable approaches.

Further research is needed to conclusively determine which physiological processes or fluxes are isolated by this new approach. Direct flux measurements from the understory, chamber studies, or isotopic tracers such as $^{13}CO_2$ (e.g., Oikawa et al., 2017) could help distinguish between photosynthetic and respiratory contributions. Additionally, conditional sampling based on tracers like COS or specific VOCs could aid in attributing CO_2 fluxes to autotrophic or heterotrophic sources. However, successful application would require identifying tracers predominantly produced by a single process or source (e.g., plants or soil microorganisms). Finally, resolving contributions from different canopy layers remains a significant challenge in ecosystems with both overstory and understory vegetation.

5. Conclusions

We proposed and evaluated a novel CO_2 flux partitioning method, Discrete Wavelet–Conditional Sampling (DW-CS), using multi-year eddy covariance datasets from a temperate mixed forest (FR-Fon) and a cropland (FR-Gri) in the Paris Basin, France. The method leverages discrete wavelet transforms to isolate scale-dependent fluctuations and applies conditional sampling based on water vapour flux to partition net CO_2 exchange into its positive (F^+) and negative (F^-) components. The central empirical assumption, that wavelet decomposition enables separation of positive and negative turbulent "gusts" otherwise entangled in the raw signal, is supported by distinct co-spectral signatures between the components, particularly under neutral and unstable atmospheric conditions.

DW-CS partitioned fluxes compared favourably to gross primary productivity (GPP) and ecosystem respiration (Reco) estimates derived from the widely used nighttime (NT) method, yielding lower mean absolute errors than both the NT–DT comparison and the inherent NEE random uncertainty. Notably, F^+ displayed a diel pattern that diverged from the temperature-driven Reco estimates of standard models. During periods of high productivity, F^+ aligned more closely with radiation, echoing patterns previously observed in chamber studies. This radiation sensitivity could reflect differentiated temperature responses of soil and plant respiration, light inhibition effects, or temporal lags between photosynthesis and the export of photosynthates to the rhizosphere. While these hypotheses remain to be tested, the DW-CS pattern points to the need for a closer examination of assumed diel respiration dynamics in carbon cycle models.

In contrast to recent model-assisted approaches (e.g., Scanlon et al., 2019; Zahn et al., 2022), DW-CS is entirely empirical and requires no prior assumptions about water use efficiency. It builds on quadrant analysis (Scanlon and Albertson, 2001; Thomas et al., 2008) and incorporates time–frequency decomposition to better support the primary assumption that some air parcels are not thoroughly mixed but transported in separate, identifiable, confined eddies. This hypothesis is supported by the different spectral signatures from the partitioned fluxes.

Although no direct validation of diel Reco patterns was available from field measurements, our findings underscore the importance of re-evaluating this key component of the CO_2 budget. The DW-CS method enables post hoc partitioning of fluxes from existing eddy covariance datasets without the need for additional instrumentation. Future work could integrate additional tracers or multi-gas observations to refine the interpretation of F^+ and F^- and explore their ecosystem-level origins more explicitly.

Eddy covariance has improved observations and, indirectly, models for the last decades. Wavelet analysis has already been used to calculate turbulent fluxes directly. While the flux community would benefit from continued and comprehensive comparisons between conventional and wavelet-based EC methods, these foundational studies, such as the present study, lay the groundwork for developing application-focused research. The simplicity and flexibility of DW-CS also make it very easy to do (re)analysis. The DW-CS approach represents a promising advancement in direct CO_2 flux partitioning, grounded in turbulence theory and trace gas co-emission, and holds significant potential for scaling up ecosystem carbon monitoring.

Data availability

Code for the wavelet analysis and partitioning method proposed in this paper is available online and can be accessed at https://doi.org/10.5281/zenodo.13844043 (Herig Coimbra, 2024) or directly as a Python library named waveletec. Data used can be requested at any time and raw data can be recovered in ICOS Data Portal (Dufrêne and Berveiller, 2018; Loubet et al., 2020).

CRediT authorship contribution statement

Pedro Henrique H. Coimbra: Writing – review & editing, Writing – original draft, Visualization, Software, Methodology, Formal analysis, Conceptualization. **Benjamin Loubet:** Writing – review & editing, Writing – original draft, Methodology, Formal analysis, Conceptualization. **Olivier Laurent:** Conceptualization. **Matthias Mauder:** Writing – review & editing, Conceptualization. **Bernard Heinesch:** Writing – review & editing, Conceptualization. **Jonathan Bitton:** Writing – review & editing. **Nicolas Delpierre:** Writing – review & editing, Data curation. **Daniel Berveiller:** Data curation. **Jérémie Depuydt:** Data curation. **Pauline Buysse:** Writing – review & editing, Data curation.

Declaration of competing interest

The authors declare that they have no known competing financial interests or personal relationships that could have appeared to influence the work reported in this paper.

Acknowledgements

We acknowledge the ICOS ERIC for providing the FR-Gri and FR-Fon data. This project has received funding from the European Union's

Horizon 2020 research and innovation programme under Grant Agreement No 101037319 (PAUL ICOS-Cities project). We are deeply grateful to the two anonymous reviewers for their insightful comments and constructive guidance, which significantly helped refine and strengthen this work. We also sincerely thank the chief editor, Georg Wohlfahrt, for his thoughtful oversight and for facilitating a rigorous and enriching review process.

Supplementary materials

Supplementary material associated with this article can be found, in the online version, at doi:10.1016/j.agrformet.2025.110684.

References

Aubinet, M., Grelle, A., Ibrom, A., Rannik, Ü., Moncrieff, J., Foken, T., Kowalski, A.S., Martin, P.H., Berbigier, P., Bernhofer, Ch., Clement, R., Elbers, J., Granier, A., Grünwald, T., Morgenstern, K., Pilegaard, K., Rebmann, C., Snijders, W., Valentini, R., Vesala, T., 1999. Estimates of the annual net carbon and water exchange of forests: the EUROFLUX methodology. In: Fitter, A.H., Raffaelli, D.G. (Eds.), Advances in Ecological Research, Advances in Ecological Research, 30. Academic Press, pp. 113–175. https://doi.org/10.1016/S0065-2504(08)60018-5.

Aubinet, M., Berbigier, P., Bernhofer, Ch., Cescatti, A., Feigenwinter, C., Granier, A., Grünwald, Th., Havrankova, K., Heinesch, B., Longdoz, B., Marcolla, B., Montagnani, L., Sedlak, P., 2005. Comparing CO2 storage and advection conditions at night at different carboeuroflux sites. Bound.-Layer Meteorol. 116, 63–93. https://doi.org/10.1007/s10546-004-7091-8.

Aubinet, M., Feigenwinter, C., Heinesch, B., Laffineur, Q., Papale, D., Reichstein, M., Rinne, J., Van Gorsel, E., 2012. Nighttime flux correction. In: Aubinet, M., Vesala, T., Papale, D. (Eds.), Eddy Covariance: A Practical Guide to Measurement and Data Analysis. Springer Netherlands, Dordrecht, pp. 133–157. https://doi.org/10.1007/978-94-007-2351-1_5.

Baldocchi, D.D., 2003. Assessing the eddy covariance technique for evaluating carbon dioxide exchange rates of ecosystems: past, present and future. Glob. Change Biol. 9, 479–492. https://doi.org/10.1046/j.1365-2486.2003.00629.x.

Berveiller, D., Dufrêne, E., Delpierre, N., Morfin, A., Vincent, G., Bazot, S., Soudani, K., Girardin, C., Guillot, T., Perot-Guillaume, C., 2024. ETC L2 ARCHIVE. Fontainebleau-Barbeau, 2019-01-01–2024-10-21.

Buysse, P., Loubet, B., DEPUYDT, J., Durand, B., Kalalian, C., 2024. ETC L2 ARCHIVE. Grignon, 2021-01-01–2024-10-01.

Canadell, J.G., Monteiro, P.M.S., Costa, M.H., Cotrim da Cunha, L., Cox, P.M., Eliseev, A. V., Henson, S., Ishii, M., Jaccard, S., Koven, C., Lohila, A., Patra, P.K., Piao, S., Rogelj, J., Syampungani, S., Zaehle, S., Zickfeld, K., 2021. Global carbon and other biogeochemical cycles and feedbacks. In: Masson-Delmotte, V., Zhai, P., Pirani, A., Connors, S.L., Péan, C., Berger, S., Caud, N., Chen, Y., Goldfarb, L., Gomis, M.I., Huang, M., Leitzell, K., Lonnoy, E., Matthews, J.B.R., Maycock, T.K., Waterfield, T., Yelekçi, O., Yu, R., Zhou, B. (Eds.), Clim. Change 2021 Phys. Sci. Basis Contrib. Work. Group Sixth Assess, Clim. Change 2021 Phys. Sci. Basis Contrib. Work. Group Sixth Assess, 673–816. Rep. Intergov. Panel Clim. Change. https://doi.org/10.1017/9781009157896.007.

Daubechies, I., 1988. Orthonormal bases of compactly supported wavelets. Commun. Pure Appl. Math. 41, 909–996. https://doi.org/10.1002/cpa.3160410705.

Daubechies, I., 1992. Ten lectures on wavelets. Soc. Ind. Appl. Math. https://doi.org/10.1137/1.9781611970104.

Delpierre, N., Berveiller, D., Granda, E., Dufrêne, E., 2016. Wood phenology, not carbon input, controls the interannual variability of wood growth in a temperate oak forest. New. Phytol. 210, 459–470. https://doi.org/10.1111/nph.13771.

Desjardins, R.L., Worth, D.E., Pattey, E., VanderZaag, A., Srinivasan, R., Mauder, M., Worthy, D., Sweeney, C., Metzger, S., 2018. The challenge of reconciling bottom-up agricultural methane emissions inventories with top-down measurements. Agric. For. Meteorol. 248, 48–59. https://doi.org/10.1016/j.agrformet.2017.09.003.

Du, Q., Liu, H., Feng, J., Wang, L., 2014. Effects of different gap filling methods and land surface energy balance closure on annual net ecosystem exchange in a semiarid area of China. Sci. China Earth. Sci. 57, 1340–1351. https://doi.org/10.1007/s11430-013-4756-5.

Duffy, K.A., Schwalm, C.R., Arcus, V.L., Koch, G.W., Liang, L.L., Schipper, L.A., 2021. How close are we to the temperature tipping point of the terrestrial biosphere? Sci. Adv. 7. https://doi.org/10.1126/sciadv.aay1052 eaay1052.

Dufrêne, E., Berveiller, D. (2018). ICOS ETC Eddy Flux Raw ASCII daily archive from Fontainebleau-Barbeau, 2018-07-04, ICOS RI, https://hdl.handle.net/11676/3hKdlUrZDxynGkEvwoeBhnMm.

Farge, M., 1992. Wavelet transforms and their applications to turbulence. Annu. Rev. Fluid. Mech. 24, 395–458.

Farge, M., Schneider, K., 2001. Analysing and Computing Turbulent Flows Using Wavelets. In: Lesieur, M., Yaglom, A., David, F. (Eds.), New Trends in Turbulence Turbulence: Nouveaux aspects: 31 July –1 September 2000, edited by. Springer, Berlin, Heidelberg, pp. 449–504. https://doi.org/10.1007/3-540-45674-0_9.

Ferrara, R.M., Loubet, B., Di Tommasi, P., Bertolini, T., Magliulo, V., Cellier, P., Eugster, W., Rana, G., 2012. Eddy covariance measurement of ammonia fluxes: comparison of high frequency correction methodologies. Agric. For. Meteorol. 158–159, 30–42. https://doi.org/10.1016/j.agrformet.2012.02.001.

Finnigan, J.J., Clement, R., Malhi, Y., Leuning, R., Cleugh, H.A., 2003. A re-evaluation of long-term flux measurement techniques part i: averaging and coordinate rotation. Bound.-Layer Meteorol. 107, 1–48. https://doi.org/10.1023/A:1021554900225.

Foken, T., Aubinet, M., Leuning, R., 2012. The Eddy Covariance Method. In: Aubinet, M., Vesala, T., Papale, D. (Eds.), Eddy Covariance: A Practical Guide to Measurement and Data Analysis. Springer Netherlands, Dordrecht, pp. 1–19. https://doi.org/10.1007/978-94-007-2351-1_1.

Foken, Th., Wichura, B., 1996. Tools for quality assessment of surface-based flux measurements. Agric. For. Meteorol. 78, 83–105. https://doi.org/10.1016/0168-1923(95)02248-1.

Fowler, D., Hargreaves, K., Skiba, U., Milne, R., Zahniser, M., Moncrieff, J., Beverland, I., Gallagher, M., 1995. Measurements of Ch4 and N2o fluxes at the landscape scale using micrometeorological methods. Philos. Trans. R. Soc. -Math. Phys. Eng. Sci. 351, 339–355. https://doi.org/10.1098/rsta.1995.0038.

Göckede, M., Kittler, F., Schaller, C., 2019. Quantifying the impact of emission outbursts and non-stationary flow on eddy-covariance CH_4 flux measurements using wavelet techniques. Biogeosciences 16, 3113–3131. https://doi.org/10.5194/bg-16-3113-2019.

van Gorsel, E., Delpierre, N., Leuning, R., Black, A., Munger, J.W., Wofsy, S., Aubinet, M., Feigenwinter, C., Beringer, J., Bonal, D., Chen, B., Chen, J., Clement, R., Davis, K.J., Desai, A.R., Dragoni, D., Etzold, S., Grünwald, T., Gu, L., Heinesch, B., Hutyra, L.R., Jans, W.W.P., Kutsch, W., Law, B.E., Leclerc, M.Y., Mammarella, I., Montagnani, L., Noormets, A., Rebmann, C., Wharton, S., 2009. Estimating nocturnal ecosystem respiration from the vertical turbulent flux and change in storage of CO2. Agric. For. Meteorol. 149, 1919–1930. https://doi.org/10.1016/j.agrformet.2009.06.020.

Goulden, M.L., Munger, J.W., Fan, S.-M., Daube, B.C., Wofsy, S.C., 1996. Measurements of carbon sequestration by long-term eddy covariance: methods and a critical evaluation of accuracy. Glob. Change Biol. 2, 169–182. https://doi.org/10.1111/j.1365-2486.1996.tb00070.x.

Gu, L., Falge, E.M., Boden, T., Baldocchi, D.D., Black, T.A., Saleska, S.R., Suni, T., Verma, S.B., Vesala, T., Wofsy, S.C., Xu, L., 2005. Objective threshold determination for nighttime eddy flux filtering. Agric. For. Meteorol. 128, 179–197. https://doi.org/10.1016/j.agrformet.2004.11.006.

Gu, L., Massman, W.J., Leuning, R., Pallardy, S.G., Meyers, T., Hanson, P.J., Riggs, J.S., Hosman, K.P., Yang, B., 2012. The fundamental equation of eddy covariance and its application in flux measurements. Agric. For. Meteorol. 152, 135–148. https://doi.org/10.1016/j.agrformet.2011.09.014.

Herig Coimbra, P.H., 2024. Wavelet-based Eddy Covariance. Zenodo. https://doi.org/10.5281/zenodo.13844043 [code].

Hoefnagel, M.H.N., Atkin, O.K., Wiskich, J.T., 1998. Interdependence between chloroplasts and mitochondria in the light and the dark. Biochim. Biophys. Acta (BBA) - Bioenerg. 1366, 235–255. https://doi.org/10.1016/S0005-2728(98)00126-1.

IPCC, 2021. Climate Change 2021: The Physical Science Basis. Contribution of Working Group I to the Sixth Assessment Report of the Intergovernmental Panel On Climate Change. In Press. https://doi.org/10.1017/9781009157896.

IPCC, 2022a. Climate Change 2022: Mitigation of Climate Change. https://doi.org/10.1017/9781009157926.

IPCC, 2022b. Climate Change 2022: Impacts, Adaptation and Vulnerability. https://doi.org/10.1017/9781009325844.

Irvin, J., Zhou, S., McNicol, G., Lu, F., Liu, V., Fluet-Chouinard, E., Ouyang, Z., Knox, S. H., Lucas-Moffat, A., Trotta, C., Papale, D., Vitale, D., Mammarella, I., Alekseychik, P., Aurela, M., Avati, A., Baldocchi, D., Bansal, S., Bohrer, G., Campbell, D.I., Chen, J., Chu, H., Dalmagro, H.J., Delwiche, K.B., Desai, A.R., Euskirchen, E., Feron, S., Goeckede, M., Heimann, M., Helbig, M., Helfter, C., Hemes, K.S., Hirano, T., Iwata, H., Jurasinski, G., Kalhori, A., Kondrich, A., Lai, D.Y., Lohila, A., Malhotra, A., Merbold, L., Mitra, B., Ng, A., Nilsson, M.B., Noormets, A., Peichl, M., Rey-Sanchez, A.C., Richardson, A.D., Runkle, B.R., Schäfer, K.V., Sonnentag, O., Stuart-Haëntjens, E., Sturtevant, C., Ueyama, M., Valach, A.C., Vargas, R., Vourlitis, G.L., Ward, E.J., Wong, G.X., Zona, D., Alberto, Ma.C.R., Billesbach, D.P., Celis, G., Dolman, H., Friborg, T., Fuchs, K., Gogo, S., Gondwe, M.J., Goodrich, J.P., Gottschalk, P., Hörtnagl, L., Jacotot, A., Koebsch, F., Kasak, K., Maier, R., Morin, T.H., Nemitz, E., Oechel, W.C., Oikawa, P.Y., Ono, K., Sachs, T., Sakabe, A., Schuur, E.A., Shortt, R., Sullivan, R.C., Szutu, D.J., Tuittila, E.-S., Varlagin, A., Verfaillie, J.G., Wille, C., Windham-Myers, L., Poulter, B., Jackson, R. B., 2021. Gap-filling eddy covariance methane fluxes: comparison of machine learning model predictions and uncertainties at FLUXNET-CH4 wetlands. Agric. For. Meteorol. 308–309, 108528. https://doi.org/10.1016/j.agrformet.2021.108528.

Järveoja, J., Nilsson, M.B., Crill, P.M., Peichl, M., 2020. Bimodal diel pattern in peatland ecosystem respiration rebuts uniform temperature response. Nat. Commun. 11, 4255. https://doi.org/10.1038/s41467-020-18027-1.

Jia, G., Shevliakova, E., Artaxo, P., De Noblet-Ducoudré, N., Houghton, R., House, J., Kitajima, K., Lennard, C., Popp, A., Sirin, A., 2019. Land–climate interactions. Climate Change and Land: an IPCC Special Report on Climate Change, Desertification, Land Degradation, Sustainable Land Management, Food Security, and Greenhouse Gas Fluxes in Terrestrial Ecosystems.

Kaimal, J.C., Finnigan, J.J., 1994. Atmospheric Boundary Layer Flows: Their Structure and Measurement. Oxford University Press, p. 304.

Keenan, T.F., Migliavacca, M., Papale, D., Baldocchi, D., Reichstein, M., Torn, M., Wutzler, T., 2019. Widespread inhibition of daytime ecosystem respiration. Nat. Ecol. Evol. 3, 407–415. https://doi.org/10.1038/s41559-019-0809-2.

Klosterhalfen, A., Graf, A., Brüggemann, N., Drüe, C., Esser, O., González-Dugo, M.P., Heinemann, G., Jacobs, C.M.J., Mauder, M., Moene, A.F., Ney, P., Pütz, T., Rebmann, C., Ramos Rodríguez, M., Scanlon, T.M., Schmidt, M., Steinbrecher, R., Thomas, C.K., Valler, V., Zeeman, M.J., Vereecken, H., 2019a. Source partitioning of H_2O and CO_2 fluxes based on high-frequency eddy covariance data: a comparison

between study sites. Biogeosciences. 16, 1111–1132. https://doi.org/10.5194/bg-16-1111-2019.
Klosterhalfen, A., Moene, A.F., Schmidt, M., Scanlon, T.M., Vereecken, H., Graf, A., 2019b. Sensitivity analysis of a source partitioning method for H2O and CO2 fluxes based on high frequency eddy covariance data: findings from field data and large eddy simulations. Agric. For. Meteorol. 265, 152–170. https://doi.org/10.1016/j.agrformet.2018.11.003.
Kowalski, A.S., Serrano-Ortiz, P., 2007. On the relationship between the eddy covariance, the turbulent flux, and surface exchange for a trace gas such as CO2. Bound.-Layer Meteorol. 124, 129–141. https://doi.org/10.1007/s10546-007-9171-z.
Lasslop, G., Reichstein, M., Papale, D., Richardson, A.D., Arneth, A., Barr, A., Stoy, P., Wohlfahrt, G., 2010. Separation of net ecosystem exchange into assimilation and respiration using a light response curve approach: critical issues and global evaluation. Glob. Change Biol. 16, 187–208. https://doi.org/10.1111/j.1365-2486.2009.02041.x.
Lee, G.R., Gommers, R., Waselewski, F., Wohlfahrt, K., O'Leary, A., 2019. PyWavelets: a Python package for wavelet analysis. J. Open. Source Softw. 4, 1237. https://doi.org/10.21105/joss.01237.
Lloyd, J., Taylor, J.A., 1994. On the temperature dependence of soil respiration. Funct. Ecol. 8, 315–323. https://doi.org/10.2307/2389824.
Loubet, B., Laville, P., Lehuger, S., Larmanou, E., Fléchard, C., Mascher, N., Genermont, S., Roche, R., Ferrara, R.M., Stella, P., Personne, E., Durand, B., Decuq, C., Flura, D., Masson, S., Fanucci, O., Rampon, J.-N., Siemens, J., Kindler, R., Gabrielle, B., Schrumpf, M., Cellier, P., 2011. Carbon, nitrogen and Greenhouse gases budgets over a four years crop rotation in northern France. Plant Soil. 343, 109. https://doi.org/10.1007/s11104-011-0751-9.
Loubet, B., Buysse, P., Gonzaga-Gomez, L., Lafouge, F., Ciuraru, R., Decuq, C., Kammer, J., Bsaibes, S., Boissard, C., Durand, B., Gueudet, J.-C., Fanucci, O., Zurfluh, O., Abis, L., Zannoni, N., Truong, F., Baisnée, D., Sarda-Estève, R., Staudt, M., Gros, V., 2022. Volatile organic compound fluxes over a winter wheat field by PTR-Qi-TOF-MS and eddy covariance. Atmospheric Chem. Phys. 22, 2817–2842. https://doi.org/10.5194/acp-22-2817-2022.
Loubet, B., Buysse, P., Durand, B. (2020). ICOS ETC Eddy Flux Raw ASCII daily archive from Grignon, 2020-12-12, ICOS RI, https://hdl.handle.net/11676/eyx4Uf7cEEzrTBfKXKDoh6X7.
Lucas-Moffat, A.M., Schrader, F., Herbst, M., Brümmer, C., 2022. Multiple gap-filling for eddy covariance datasets. Agric. For. Meteorol. 325, 109114. https://doi.org/10.1016/j.agrformet.2022.109114.
Mallat, S.G., 1989. A theory for multiresolution signal decomposition: the wavelet representation. IEEE Trans. Pattern. Anal. Mach. Intell. 11, 674–693. https://doi.org/10.1109/34.192463.
Mallat, S., 1999. VII - Wavelet bases. In: Mallat, S. (Ed.), A Wavelet Tour of Signal Processing, 2nd Edition. Academic Press, San Diego, pp. 220–320. https://doi.org/10.1016/B978-012466606-1/50009-X.
Maseyk, K., Berry, J.A., Billesbach, D., Campbell, J.E., Torn, M.S., Zahniser, M., Seibt, U., 2014. Sources and sinks of carbonyl sulfide in an agricultural field in the Southern Great Plains. Proc. Natl. Acad. Sci. 111, 9064–9069. https://doi.org/10.1073/pnas.1319132111.
Massman, W.J., Lee, X., 2002. Eddy covariance flux corrections and uncertainties in long-term studies of carbon and energy exchanges. Agric. For. Meteorol. 113, 121–144. https://doi.org/10.1016/S0168-1923(02)00105-3.
Mauder, M. and Foken, T.: Documentation and instruction manual of the eddy-covariance software package TK3, 60, 2011.
Mauder, M., Desjardins, R.L., MacPherson, I., 2007. Scale analysis of airborne flux measurements over heterogeneous terrain in a boreal ecosystem. J. Geophys. Res. Atmos. 112. https://doi.org/10.1029/2006JD008133.
Mauder, M., Cuntz, M., Drüe, C., Graf, A., Rebmann, C., Schmid, H.P., Schmidt, M., Steinbrecher, R., 2013. A strategy for quality and uncertainty assessment of long-term eddy-covariance measurements. Agric. For. Meteorol. 169, 122–135. https://doi.org/10.1016/j.agrformet.2012.09.006.
Metzger, S., 2018. Surface-atmosphere exchange in a box: making the control volume a suitable representation for in-situ observations. Agric. For. Meteorol. 255, 68–80. https://doi.org/10.1016/j.agrformet.2017.08.037.
Metzger, S., Junkermann, W., Mauder, M., Butterbach-Bahl, K., Trancón y Widemann, B., Neidl, F., Schäfer, K., Wieneke, S., Zheng, X.H., Schmid, H.P., Foken, T., 2013. Spatially explicit regionalization of airborne flux measurements using environmental response functions. Biogeosciences 10, 2193–2217. https://doi.org/10.5194/bg-10-2193-2013.
Mishurov, M., Kiely, G., 2011. Gap-filling techniques for the annual sums of nitrous oxide fluxes. Agric. For. Meteorol. 151, 1763–1767. https://doi.org/10.1016/j.agrformet.2011.07.014.
Moffat, A.M., Papale, D., Reichstein, M., Hollinger, D.Y., Richardson, A.D., Barr, A.G., Beckstein, C., Braswell, B.H., Churkina, G., Desai, A.R., Falge, E., Gove, J.H., Heimann, M., Hui, D., Jarvis, A.J., Kattge, J., Noormets, A., Stauch, V.J., 2007. Comprehensive comparison of gap-filling techniques for eddy covariance net carbon fluxes. Agric. For. Meteorol. 147, 209–232. https://doi.org/10.1016/j.agrformet.2007.08.011.
Moncrieff, J.B., Massheder, J.M., de Bruin, H., Elbers, J., Friborg, T., Heusinkveld, B., Kabat, P., Scott, S., Soegaard, H., Verhoef, A., 1997. A system to measure surface fluxes of momentum, sensible heat, water vapour and carbon dioxide. J. Hydrol. 188–189, 589–611. https://doi.org/10.1016/S0022-1694(96)03194-0.
Oikawa, P.Y., Sturtevant, C., Knox, S.H., Verfaillie, J., Huang, Y.W., Baldocchi, D.D., 2017. Revisiting the partitioning of net ecosystem exchange of CO2 into photosynthesis and respiration with simultaneous flux measurements of 13CO2 and CO2, soil respiration and a biophysical model. CANVEG Agric. For. Meteorol. 234–235, 149–163. https://doi.org/10.1016/j.agrformet.2016.12.016.
Papale, D., Reichstein, M., Aubinet, M., Canfora, E., Bernhofer, C., Kutsch, W., Longdoz, B., Rambal, S., Valentini, R., Vesala, T., Yakir, D., 2006. Towards a standardized processing of Net Ecosystem Exchange measured with eddy covariance technique: algorithms and uncertainty estimation. Biogeosciences 3, 571–583. https://doi.org/10.5194/bg-3-571-2006.
Pärnik, T., Keerberg, O., 1995. Decarboxylation of primary and end products of photosynthesis at different oxygen concentrations. J. Exp. Bot. 46, 1439–1477.
Pastorello, G., Trotta, C., Canfora, E., Chu, H., Christianson, D., Cheah, Y.-W., Poindexter, C., Chen, J., Elbashandy, A., Humphrey, M., Isaac, P., Polidori, D., Reichstein, M., Ribeca, A., van Ingen, C., Vuichard, N., Zhang, L., Amiro, B., Ammann, C., Arain, M.A., Ardö, J., Arkebauer, T., Arndt, S.K., Arriga, N., Aubinet, M., Aurela, M., Baldocchi, D., Barr, A., Beamesderfer, E., Marchesini, L.B, Bergeron, O., Beringer, J., Bernhofer, C., Berveiller, D., Billesbach, D., Black, T.A., Blanken, P.D., Bohrer, G., Boike, J., Bolstad, P.V., Bonal, D., Bonnefond, J.-M., Bowling, D.R., Bracho, R., Brodeur, J., Brümmer, C., Buchmann, N., Burban, B., Burns, S.P., Buysse, P., Cale, P., Cavagna, M., Cellier, P., Chen, S., Chini, I., Christensen, T.R., Cleverly, J., Collalti, A., Consalvo, C., Cook, B.D., Cook, D., Coursolle, C., Cremonese, E., Curtis, P.S., D'Andrea, E., da Rocha, H., Dai, X., Davis, K.J., Cinti, B.D., Grandcourt, A.de, Ligne, A.D., De Oliveira, R.C., Delpierre, N., Desai, A.R., Di Bella, C.M., Tommasi, P.di, Dolman, H., Domingo, F., Dong, G., Dore, S., Duce, P., Dufrêne, E., Dunn, A., Dušek, J., Eamus, D., Eichelmann, U., ElKhidir, H.A.M., Eugster, W., Ewenz, C.M., Ewers, B., Famulari, D., Fares, S., Feigenwinter, I., Feitz, A., Fensholt, R., Filippa, G., Fischer, M., Frank, J., Galvagno, M., et al., 2020. The FLUXNET2015 dataset and the ONEFlux processing pipeline for eddy covariance data. Sci. Data 7, 225. https://doi.org/10.1038/s41597-020-0534-3.
Perez-Priego, O., Katul, G., Reichstein, M., El-Madany, T.S., Ahrens, B., Carrara, A., Scanlon, T.M., Migliavacca, M., 2018. Partitioning eddy covariance water flux components using physiological and micrometeorological approaches. J. Geophys. Res. Biogeosciences 123, 3353–3370. https://doi.org/10.1029/2018JG004637.
Poggi, D., Porporato, A., Ridolfi, L., Albertson, J.D., Katul, G.G., 2004. The effect of vegetation density on canopy sub-layer turbulence. Bound. Layer Meteorol. 111, 565–587. https://doi.org/10.1023/B:BOUN.0000016576.05621.73.
Pohl, F., Rakovec, O., Rebmann, C., Hildebrandt, A., Boeing, F., Hermanns, F., Attinger, S., Samaniego, L., Kumar, R., 2023. Long-term daily hydrometeorological drought indices, soil moisture, and evapotranspiration for ICOS sites. Sci. Data 10, 281. https://doi.org/10.1038/s41597-023-02192-1.
Polonik, P., Chan, W.S., Billesbach, D.P., Burba, G., Li, J., Nottrott, A., Bogoev, I., Conrad, B., Biraud, S.C., 2019. Comparison of gas analyzers for eddy covariance: effects of analyzer type and spectral corrections on fluxes. Agric. For. Meteorol. 272, 128–142.
Rana, G., Palatella, L., Scanlon, T.M., Martinelli, N., Ferrara, R.M., 2018. CO2 and H2O flux partitioning in a Mediterranean cropping system. Agric. For. Meteorol. 260–261, 118–130. https://doi.org/10.1016/j.agrformet.2018.06.007.
Rannik, Ü., Vesala, T., 1999. Autoregressive filtering versus linear detrending in estimation of fluxes by the eddy covariance method. Bound.-Layer Meteorol. 91, 259–280. https://doi.org/10.1023/A:1001840416858.
Rebmann, C., Aubinet, M., Schmid, H., Arriga, N., Aurela, M., Burba, G., Clement, R., De Ligne, A., Fratini, G., Gielen, B., Grace, J., Graf, A., Gross, P., Haapanala, S., Herbst, M., Hörtnagl, L., Ibrom, A., Joly, L., Kljun, N., Franz, D., 2018. ICOS eddy covariance flux-station site setup: a review. Int. Agrophysics 32, 471–494. https://doi.org/10.1515/intag-2017-0044.
Reichstein, M., Falge, E., Baldocchi, D., Papale, D., Aubinet, M., Berbigier, P., Bernhofer, C., Buchmann, N., Gilmanov, T., Granier, A., Grünwald, T., Havránková, K., Ilvesniemi, H., Janous, D., Knohl, A., Laurila, T., Lohila, A., Loustau, D., Matteucci, G., Meyers, T., Miglietta, F., Ourcival, J.-M., Pumpanen, J., Rambal, S., Rotenberg, E., Sanz, M., Tenhunen, J., Seufert, G., Vaccari, F., Vesala, T., Yakir, D., Valentini, R., 2005. On the separation of net ecosystem exchange into assimilation and ecosystem respiration: review and improved algorithm. Glob. Change Biol. 11, 1424–1439. https://doi.org/10.1111/j.1365-2486.2005.001002.x.
Reichstein, M., Stoy, P.C., Desai, A.R., Lasslop, G., Richardson, A.D., 2012. Partitioning of net fluxes. In: Aubinet, M., Vesala, T., Papale, D. (Eds.), Eddy Covariance: A Practical Guide to Measurement and Data Analysis. Springer Netherlands, Dordrecht, pp. 263–289. https://doi.org/10.1007/978-94-007-2351-1_9.
Sabbatini, S., Mammarella, I., Arriga, N., Fratini, G., Graf, A., Hörtnagl, L., Ibrom, A., Longdoz, B., Mauder, M., Merbold, L., Metzger, S., Montagnani, L., Pitacco, A., Rebmann, C., Sedlák, P., Šigut, L., Vitale, D., Papale, D., 2018. Eddy covariance raw data processing for CO2 and energy fluxes calculation at ICOS ecosystem stations. Int. Agrophysics 32, 495–515. https://doi.org/10.1515/intag-2017-0043.
Scanlon, T.M., Albertson, J.D., 2001. Turbulent transport of carbon dioxide and water vapor within a vegetation canopy during unstable conditions: identification of episodes using wavelet analysis. J. Geophys. Res.: Atmos. 106, 7251–7262. https://doi.org/10.1029/2000JD900662.
Scanlon, T.M., Kustas, W.P., 2010. Partitioning carbon dioxide and water vapor fluxes using correlation analysis. Agric. For. Meteorol. 150, 89–99. https://doi.org/10.1016/j.agrformet.2009.09.005.
Scanlon, T.M., Kustas, W.P., 2012. Partitioning evapotranspiration using an eddy covariance-based technique: improved assessment of soil moisture and land–atmosphere exchange dynamics. Vadose Zone J. 11, vzj2012. https://doi.org/10.2136/vzj2012.0025, 0025.
Scanlon, T.M., Sahu, P., 2008. On the correlation structure of water vapor and carbon dioxide in the atmospheric surface layer: a basis for flux partitioning. Water Resour. Res. 44. https://doi.org/10.1029/2008WR006932.

Scanlon, T.M., Schmidt, D.F., Skaggs, T.H., 2019. Correlation-based flux partitioning of water vapor and carbon dioxide fluxes: method simplification and estimation of canopy water use efficiency. Agric. For. Meteorol. 279, 107732. https://doi.org/10.1016/j.agrformet.2019.107732.

Schaller, C., Göckede, M., Foken, T., 2017. Flux calculation of short turbulent events - comparison of three methods. Atmos. Meas. Tech. 10, 869–880. https://doi.org/10.5194/amt-10-869-2017.

Sousa, P.M., Barriopedro, D., García-Herrera, R., Ordóñez, C., Soares, P.M.M., Trigo, R. M., 2020. Distinct influences of large-scale circulation and regional feedbacks in two exceptional 2019 European heatwaves. Commun. Earth Environ. 1, 1–13. https://doi.org/10.1038/s43247-020-00048-9.

Strunin, M.A., Hiyama, T., 2004. Applying wavelet transforms to analyse aircraft-measured turbulence and turbulent fluxes in the atmospheric boundary layer over eastern Siberia. Hydrol. Process. 18, 3081–3098. https://doi.org/10.1002/hyp.5750.

Sulman, B.N., Roman, D.T., Scanlon, T.M., Wang, L., Novick, K.A., 2016. Comparing methods for partitioning a decade of carbon dioxide and water vapor fluxes in a temperate forest. Agric. For. Meteorol. 226–227, 229–245. https://doi.org/10.1016/j.agrformet.2016.06.002.

Super, I., Denier van der Gon, H.A.C., Visschedijk, A.J.H., Moerman, M.M., Chen, H., van der Molen, M.K., Peters, W., 2017. Interpreting continuous in-situ observations of carbon dioxide and carbon monoxide in the urban port area of Rotterdam. Atmos. Pollut. Res. 8, 174–187. https://doi.org/10.1016/j.apr.2016.08.008.

Thomas, C., Foken, T., 2002. *Re*-evaluation of integral turbulence characteristics and their parameterisations. In: 15th Symposium on Boundary Layers and Turbulence. Boston, pp. 129–132.

Thomas, C., Martin, J.G., Goeckede, M., Siqueira, M.B., Foken, T., Law, B.E., Loescher, H. W., Katul, G., 2008. Estimating daytime subcanopy respiration from conditional sampling methods applied to multi-scalar high frequency turbulence time series. Agric. For. Meteorol. 148, 1210–1229. https://doi.org/10.1016/j.agrformet.2008.03.002.

Torrence, C., Compo, G.P., 1998. A practical guide to wavelet analysis. Bull. Am. Meteorol. Soc. 79, 61–78. https://doi.org/10.1175/1520-0477(1998)079<0061:APGTWA>2.0.CO;2.

Valentini, R., De ANGELIS, P., Matteucci, G., Monaco, R., Dore, S., Mucnozza, G.E.S., 1996. Seasonal net carbon dioxide exchange of a beech forest with the atmosphere. Glob. Change Biol. 2, 199–207. https://doi.org/10.1111/j.1365-2486.1996.tb00072.x.

Vekuri, H., Tuovinen, J.-P., Kulmala, L., Papale, D., Kolari, P., Aurela, M., Laurila, T., Liski, J., Lohila, A., 2023. A widely-used eddy covariance gap-filling method creates systematic bias in carbon balance estimates. Sci. Rep. 13. https://doi.org/10.1038/s41598-023-28827-2.

Voyard, A., Ciuraru, R., Lafouge, F., Decuq, C., Fortineau, A., Loubet, B., Staudt, M., Rees, F., 2024. Emissions of volatile organic compounds from aboveground and belowground parts of rapeseed (Brassica napus L.) and tomato (Solanum lycopersicum L.). Sci. Total Environ. 955, 177081. https://doi.org/10.1016/j.scitotenv.2024.177081.

Wang, W., Smith, J.A., Ramamurthy, P., Baeck, M.L., Bou-Zeid, E., Scanlon, T.M., 2016. On the correlation of water vapor and CO2: application to flux partitioning of evapotranspiration. Water Resour. Res. 52, 9452–9469. https://doi.org/10.1002/2015WR018161.

Webb, E.K., Pearman, G.I., Leuning, R., 1980. Correction of flux measurements for density effects due to heat and water vapour transfer. Q. J. R. Meteorol. Soc. 106, 85–100. https://doi.org/10.1002/qj.49710644707.

Wehr, R., Munger, J.W., McManus, J.B., Nelson, D.D., Zahniser, M.S., Davidson, E.A., Wofsy, S.C., Saleska, S.R., 2016. Seasonality of temperate forest photosynthesis and daytime respiration. Nature 534, 680–683. https://doi.org/10.1038/nature17966.

Wilczak, J.M., Oncley, S.P., Stage, S.A., 2001. Sonic anemometer tilt correction algorithms. Bound.-Layer Meteorol. 99, 127–150. https://doi.org/10.1023/A:1018966204465.

Wohlfahrt, G., Bahn, M., Haslwanter, A., Newesely, C., Cernusca, A., 2005. Estimation of daytime ecosystem respiration to determine gross primary production of a mountain meadow. Agric. For. Meteorol. 130, 13–25. https://doi.org/10.1016/j.agrformet.2005.02.001.

Wohlfahrt, G., Galvagno, M., 2017. Revisiting the choice of the driving temperature for eddy covariance CO2 flux partitioning. Agric. For. Meteorol. 237–238, 135–142. https://doi.org/10.1016/j.agrformet.2017.02.012.

Wohlfahrt, G., Gu, L., 2015. The many meanings of gross photosynthesis and their implication for photosynthesis research from leaf to globe. Plant Cell Environ. 38, 2500–2507. https://doi.org/10.1111/pce.12569.

Wutzler, T., Lucas-Moffat, A., Migliavacca, M., Knauer, J., Sickel, K., Šigut, L., Menzer, O., Reichstein, M., 2018. Basic and extensible post-processing of eddy covariance flux data with REddyProc. Biogeosciences 15, 5015–5030. https://doi.org/10.5194/bg-15-5015-2018.

Zahn, E., Bou-Zeid, E., Good, S.P., Katul, G.G., Thomas, C.K., Ghannam, K., Smith, J.A., Chamecki, M., Dias, N.L., Fuentes, J.D., Alfieri, J.G., Kwon, H., Caylor, K.K., Gao, Z., Soderberg, K., Bambach, N.E., Hipps, L.E., Prueger, J.H., Kustas, W.P., 2022. Direct partitioning of eddy-covariance water and carbon dioxide fluxes into ground and plant components. Agric. For. Meteorol. 315, 108790. https://doi.org/10.1016/j.agrformet.2021.108790.

Zahn, E., Ghannam, K., Chamecki, M., Moene, A.F., Kustas, W.P., Good, S., Bou-Zeid, E., 2024. Numerical investigation of observational flux partitioning methods for water vapor and carbon dioxide. J. Geophys. Res.: Biogeosciences 129, e2024JG008025. https://doi.org/10.1029/2024JG008025.

Zeeman, M.J., Eugster, W., Thomas, C.K., 2013. Concurrency of coherent structures and conditionally sampled daytime sub-canopy respiration. Bound.-Layer Meteorol. 146, 1–15. https://doi.org/10.1007/s10546-012-9745-2.

Zhu, W., van Hout, R., Katz, J., 2007. On the flow structure and turbulence during sweep and ejection events in a wind-tunnel model canopy. Bound.-Layer Meteorol. 124, 205–233. https://doi.org/10.1007/s10546-007-9174-9.